Fabrication of Gold Nano-Particle Based Sensors Using Microspotting and DEP Technologies

LEUNG, Siu Ling

A Thesis Submitted in Partial Fulfilment

of the Requirements for the Degree of

Master of Philosophy

in

Automation and Computer-Aided Engineering

March 2009

Thesis/ Assessment Committee

Professor Du, Ruxu (Chair)
Professor Li, Wen Jung (Thesis Supervisor)
Professor Liao, Wei-Hsin (Committee Member)
Professor Tseng, Fan-Gang (External Examiner)

Fabrication of Gold Nano-Particle Based Sensors Using Microspotting and DEP Technologies

Submitted by
Siu Ling LEUNG
for the degree of Master of Philosophy
at The Chinese University of Hong Kong in Dec 2008

Abstract

In this dissertation, we have shown that an Au pearl chain (PC) can be formed consistently between microelectrodes by combining microspotting and DEP technologies. To achieve the optimum formation rate of gold pearl chains, both theoretical and experimental studies are presented. Experiments on varying the Au particle size and dielectrophoretic (DEP) parameters, including voltage and frequency, are performed in order to explore the critical parameters in controlling the Pearl Chain Formation (PCF) process between microelectrodes. Theoretical analysis was carried out by applying the theories of DEP force and AC electrokinetics to explain the experimental observations within the DEP frequency ranging from 1Hz to 10MHz. To minimize the production time and cost of Au pearl chain formation (PCF), we have combined DEP Au PC batch manipulation and microspotting technology. A computer-controlled microspotting system was previously developed, which allows controlled volumes of solutions to be precisely spotted across the microelectrodes, resulting in a high yield and high precision rapid assembly method for Au pearl chains. Finally, the properties of Au pearl chains, which include I-V characteristics and thermal sensitivities, are studied. The TCR of Au pearl chains indicate that these Au pearl chains could potentially be used to sense temperature and other thermally based physical phenomena. In this work, the Au pearl chains are found to be novel sensing elements for low power thermal and airflow sensors.

摘要

本論文主要研究金納米粒子（AuNPs）鏈及感應器的製造方法。從理論和實驗角度分析出有效操控介電泳（DEP）技術生產金納米粒子鏈的條件及方法。由於在非均勻電場環境下納米顆粒不單受DEP力所影響，同時亦會被非均勻電場所產生液的流體運動推動。有見及此，本論文更運用電液動力學就實驗結果作多方面的分析。為減低生產時間和成本，本研究結合了介電泳及微點滴技術。從而研發出一個高精密度及快速的金納米粒子鏈裝配方法。最後，本論文就金納米粒子鏈的特性作進一步的研究。其熱敏應性反應出金納米粒子鏈可被用作檢測溫度轉變或其他與溫度有關的物理現象。總括而言，本研究成功研發出以金納米粒子鏈為建基的低能量熱或氣流傳感器。

Acknowledgement

This research work would not have been possible without the help and support of many people. I would like to extend my gratitude to my supervisor Prof. Wen J. Li for his guidance, valuable discussion and patience. Especially, I would like to thank him for all the opportunities he gave me, not only in learning the research methodologies but also in personal growth.

Special thanks go to Dr. Yanli Qu and Dr. Winnie W.Y. Chow for their useful discussions and encouragements. Ms. Mandy L.Y. Sin has taught me all the basic skills from the very beginning. Deep thanks go to our collaborator Mr. Minglin Li for his meaningful discussions and simulations.

I would also want to thank all members in CMNS, especially Ms. Heidi Wong and Ms. Amy Hiew for all the useful techniques they have taught me in management, graphic design, etc. Thanks again to all CMNS members for giving me a memorial and joyful Mphil period.

Furthermore, I would like to thank Dr. Cheung in the Department of Electrical Engineering and Andrew Li in the Department of Physics for their technical support.

Last but not least, my deepest gratitude is due to my parents. They have used all their patience and effort to bring me up and help me fight against illness. Lastly, thank you Elaine and Rainbow for giving me joy and fun in my lifetime.

Table of Contents

List of Figures

1. Introduction

1.1 Background

Gold nanoparticles (AuNPs) or colloidal particles have been extensively studied because of their remarkable properties, such as high electrical conductivity, small diffusion time [1][2], high capture efficiency and fast response time [3]. The absorption characteristics of the gold NPs immobilize enzymes and metalloprotein on AuNPs or gold nanowires (NWs), indicate that AuNP based devices can potentially work in bio-sensing applications [4-8]. Recently, researchers have demonstrated different kinds of AuNP based biosensors, for example, immobilizing cholesterol oxidase on gold nanowire for cholesterol detection in blood [9] and functionalized AuNPs with methyl-3-mercaptopropionate (MMP) to detect acetic acid [10]. Furthermore, because of the photonic properties of AuNPs, detection of conformational change and environmental contaminants become feasible by obtaining the absorbance spectrum of AuNP based devices using colorimetric sensors [11]. In conclusion, AuNP based sensors serve potential applications in the area of nano-medicine [12][13], nano-photonics [14] and nano-devices fabrication [15].

In the AuNP based sensors, gold nanowire or pearl chain serve as an essential sensing element. To fabricate the nanowire/ pearl chain, varieties of fabrication techniques have been developed in the past few decades. One common methodology of nanowire growth is the vapour-liquid-solid (VLS) synthesis method first reported in 1964 by Wanger and Ellis [16]. Another ordinary nanowire fabrication method is using an atomic force microscope. The oscillating tip coated with gold comes close to the substrate and gold atoms are transported to specific locations by controlling the applied voltage [17][18]. Lastly, electron beam lithography or nanoskiving methodology is widely used to fabricate nanowires with specific dimensions [19][20]. However, all the above methodologies require precision control and take several steps to fabricate a gold nanowire. In this work, dielectrophoretic (DEP) technique is used to manipulate gold nanoparticles directly [13][21]. Compare with other fabrication techniques, the DEP technique reduces the formation time and procedure since this technique assembles nanowires in a single step [22], in which dielectric particles, e.g. gold nanoparticles, experience a force enhanced by a non-uniform electric field as a result of polarization.

The DEP technique fabricates gold nanowire through manipulation of the gold nanospheres and the AuNPs link together one by one to form the nanowire structure, which is also known as the gold pearl chain. The ability of an electric field is not only to generate the DEP force, but also to induce AC electroosmosis and AC electrokinetics fluid flow. AC electroosmosis is induced because of the interaction between ions/molecules in the solution and electrode surface. AC electrokinetics fluid flow happens as a large power density is generated in the fluid surrounding the electrodes when a high electric field is applied to manipulate small particles [23]. The influence of fluid motion on the AuNP manipulation process depends on the parameters of input signal and solution conductivities. To explore the critical condition for pearl chain formation, parametric experimental studies are performed, followed by theoretical analysis. A systematic study of gold pearl chain formation (PCF) by DEP force is presented in this dissertation. Lastly, the properties of the gold pearl chain are studied in order to investigate its potential application. Its thermal sensitivities show that the pearl chain can potentially work as a temperature sensor or other thermal-based physical phenomena sensor.

1.2 Objective

The gold nanowire/pearl chain is an essential element in micro/nano-devices to serve as the sensing element or building block. The sensor responsibility is increased by the nanowire/pearl chain structure in certain applications, e.g. gas flow detection. Moreover, the AuNP based sensor is comparably stable than sensors formed by other materials e.g. EG-CNTs. The objective of this project is to fabricate an AuNP based sensor effectively by combining DEP and microspotting technology. The first focus of this project is to prove that the integration of technologies is feasible for fabricating the gold pearl chain. The second focus is controlling pearl chain formation and analyzing the critical parameters for formation. Experiments on varying the gold particle size and DEP parameters are performed. With theoretical analysis of DEP force and AC electrokinetics, the critical parameters are achieved. Lastly, the properties of the Au pearl chain are studied and the application of the sensor is investigated, in order to achieve the ultimate goal of developing a gold nano-particle based sensor.

1.3 Organization of the Thesis

In this dissertation, the overview of gold nanoparticles and definition of different kinds of forces involved in DEP manipulation are explained in Chapter 2. Theoretical calculation in fluid velocity induced by AC electrokinetics and particle velocity induced by DEP force are simulated and compared in Chapter 3. Chapter 4 introduces the fabrication procedure and experimental setup for pearl chain formation. Moreover, the experimental results and image of the pearl chain are also shown in this section. The experimental results are analyzed in Chapter 5 in order to explore the optimal condition for PCF.

After successfully demonstrating that AuNP based pearl chains can form between microelectrodes, their characteristics such as I-V curve are studied in Chapter 6. Based on the thermal properties of the gold pearl chain, an airflow sensor is developed. The analyses of the airflow sensing results together with the experimental setup are presented in Chapter 7. Finally, a project conclusion and future work are given in Chapter 8 and Chapter 9 respectively.

2. Literature Review

2.1 Overview of Colloidal Gold

Colloidal gold has been used since Ancient Roman times for glass colouring. Recently, it has extensively been used in medicine and engineering. Medically, it is used for drug delivery [24], disease targeting and curing [25][26]. In engineering, it serves as the raw material for developing MEMS devices because of its remarkable properties as described in Section 1.1. Colloidal gold is defined as spherical gold nanoparticles suspended in a liquid medium - usually water. The colour of the solution depends on the size of the nanoparticles, which varies from wine red (for particles smaller than 100nm) to dirty yellow (for larger particles) [27]. For particles around 2nm, the solution appears colourless. Two common methodologies for fabricating colloidal gold include Turkevich *et al.'s* method and Brust *et al.'s* method [28]. Basically, colloidal gold is produced by reduction of chloroauric acid ($H[AuCl_4]$). Chloroauric acid mixes with a reducing agent to reduce Au^{3+}ions to Au atoms. When the solution is supersaturated with Au atoms, sub-nanometer particles are precipitated in the solution. The uniformity and size of the particles depends on the vigour of stirring. To prevent aggregation of the nanoparticles, chemical stabilizer, e.g. sodium citrate or TOAB is added to the solution. The particles are considered a single shell model in calculations because of having a protective layer. In our experiment, EM, a GC series colloidal solution purchased from British Biocell International, Cardiff, UK is used.

2.2 Dielectrophoresis (DEP)

Under uniform electric fields, particles remain stable since the net force acting on each particle is zero (as shown in Figure 1). On the other hand, under non-uniform electric fields, particles move toward either strong or weak electric field regions. Dielectrophoresis (DEP) is defined as the lateral motion generated on uncharged particles due to polarization induced by non-uniform electric fields [22]. As shown in Figure 2, if the particle is more polarized than the medium, particles move towards the strong electric field region and experience a positive DEP force. Negative DEP force is generated if a particle is less polarized than the medium and the particle will move towards the weak electric field region.

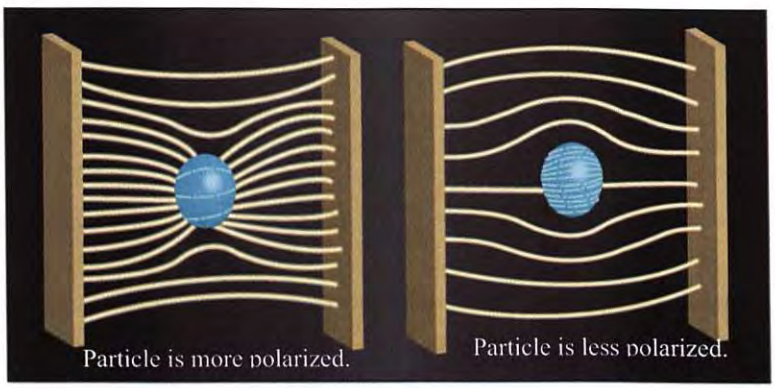

Figure 1 Electric field distribution around a particle for a uniform field

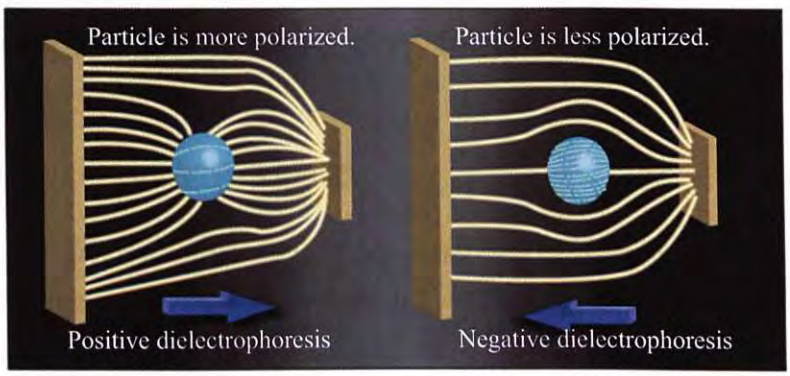

Figure 2 Electric field distribution around a particle for a non-uniform field

The Dielectrophoresis (DEP) force exerted on spherical particles can be expressed as:

$$< F_{DEP}(t) >= 2\pi\varepsilon_m a^3 \,\mathrm{Re}[K(\omega)]\nabla \mid E_{rms} \mid^2 \qquad (1)$$

where ε_m is the dielectric permittivity of the medium, a is the radius of the particle, ω is the angular frequency, E_{rms} is the RMS of electric field intensity and K is the Clausius-Mossoti (CM) factors which is given by:

$$K(\omega) = \frac{\varepsilon_p^* - \varepsilon_m^*}{\varepsilon_p^* - 2\varepsilon_m^*} \qquad (2)$$

where ε_p^* and ε_m^* are the complex permittivity of the particle and the medium respectively. The complex permittivity is given by:

$$\varepsilon^* = \varepsilon - j\frac{\sigma}{\omega} \qquad (3)$$

where σ is the conductivities of the medium [23].

For spherical particles, the particle velocity induced by DEP force is given by:

$$v_{DEP} = \frac{F_{DEP}}{6\pi\eta r} \quad (4)$$

where η is the viscosity of the medium [32].

The magnitude of dielectrophoresis force is determined by the magnitudes of the applied electric field intensity and physical dimensions of NPs, whereas the real part of the CM factor determines the direction of the dielectrophoresis force. If the real part of the CM factor is positive, positive DEP force is generated. NPs move towards a strong electric field region and are drawn downwards to the edges of the electrodes. Negative DEP force is generated when the real part of the CM factor is negative and particles move towards the weak electric field region [13].

2.2.1 CM factor of Single Shell Model

In DEP manipulation, the real part of the Clausius-Mossoti (CM) factor governs the direction of the particle movement and it varies from -0.5 to 1.0 for spherical particles, whereas the imaginary part of the CM factor determines the electro-rotational torque of particles in electrokinetic manipulation [29]. Figure 41 in Appendix-I shows the CM factor of a homogeneous dielectric sphere. However, in our experiment, gold nano-particles are considered a single shell model instead of a homogeneous sphere since the particles are coated with chemical stabilizer to prevent aggregation among particles. The CM factor of the single shell model is different from the one for a homogeneous sphere since the effective permittivity of single shell particles is different, and is given by [30]:

$$\varepsilon_m^* = c_m R\left[\frac{j\omega\tau_c + 1}{j\omega(\tau_m + \tau_c) + 1}\right] \quad (5)$$

where $\tau_s = c_s R/\sigma_c$ and $\tau_c = \varepsilon_c/\sigma_c$.

Assuming that the surface transmembrane conductance g_m is negligible, substituting equation (5) into (2) the complex CM factor becomes:

$$K(\omega) = -\left[\frac{\omega^2(\tau_s\tau_m + \tau_c\tau_m') + j\omega(\tau_m' - \tau_m - \tau_s) - 1}{\omega^2(2\tau_m\tau_s + \tau_c\tau_m') - j\omega(\tau_m' + \tau_m + 2\tau_s) - 2}\right] \quad (6)$$

where $\tau'_m = c_s R/\sigma_m$ and $\tau_m = \varepsilon_m/\sigma_m$.

Equation (6) shows that the CM factor of the single shell model is strongly inferred by the particle size, surface conductivity of the thin surface layer, external medium conductivity, external medium permittivity, core sphere conductivity and core sphere permittivity. The detail of each factor is demonstrated in Figure 3. The trend of the real part of the CM factor for a single shell model among various frequencies is convex-shaped with a peak at a specific frequency which depends on the above six factors. A detailed simulation on the effect of each factor will be presented in section I-2 of Appendix-I.

In conclusion, the frequency range which positive DEP force encounter by homogeneous dielectric sphere and single shell particles is absolutely different. Positive DEP force induced on homogeneous dielectric sphere in either low frequency or high frequency range, which depends on the permittivity and conductivities of the core sphere and the thin surface layer. Detail is shown in Appendix I. Moreover, the magnitude of DEP force is almost the same within either high or low frequency region. The magnitude only varies in the frequency range that the CM factor switches its direction. For single shell particles, positives DEP force induces in a particular frequency range, which depends on the six parameters as shown in Figure 3. The magnitude of DEP force act on single shell particles varies among frequencies and achieves a maximum at a specific frequency.

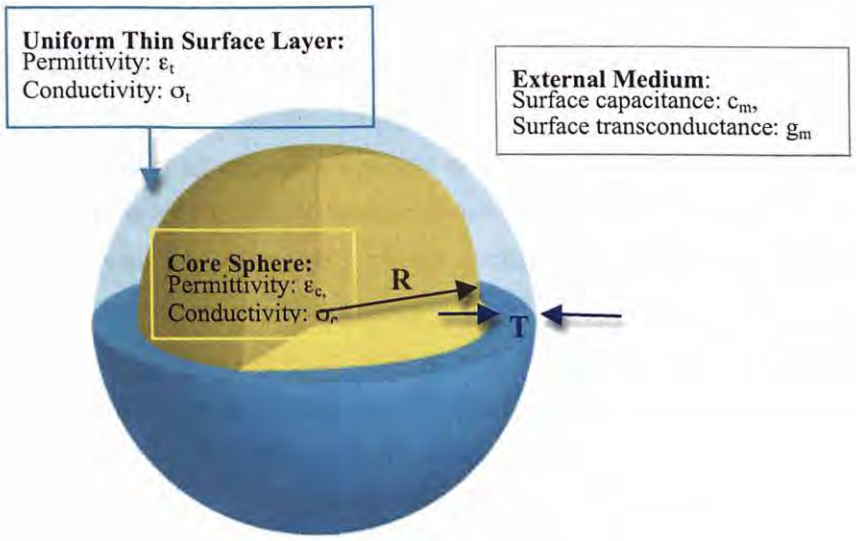

Figure 3 Dielectric model of a single shell particle

2.3 Double Layer and AC Electroosmosis

2.3.1 Double Layer

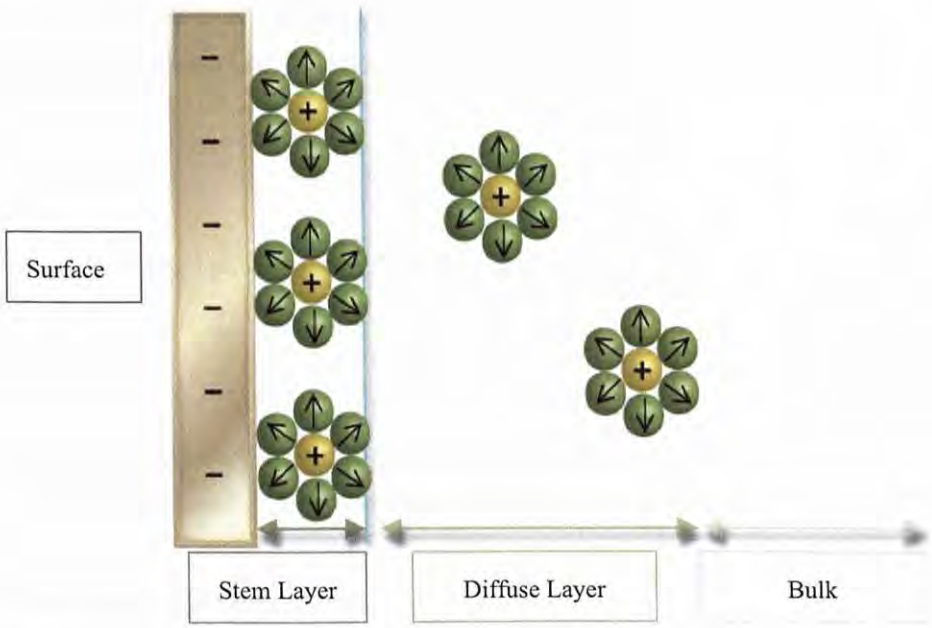

Figure 4 Diagram illustrating the structure of the double layer of a charged surface [32]

A double layer is induced by the electrostatic potential attracting ions of opposite charge in solution and repelling ions with like charge. When a surface is being charged, the region of the liquid near to the charged surface contains more counterions than the bulk. These layers are known as stem layer and diffuse layer, as shown in Figure 4. The stem layer is of one to two ions thick, which is comparably closely packed compared to the diffuse layer. A combination of these layers is called the double layer. The behaviour of the double layer in electrode-electrode systems can be understood as a circuit with a set of parallel-connected resistor and capacitor in between two sets of resistor and capacitor connected in series. The potential drop across the double layer can be derived as [32]:

$$\Delta\phi_{DL} = \frac{\phi_o}{2 + i\omega\pi(\varepsilon_m/\sigma)\kappa x} \qquad (7)$$

where ϕ_o is the applied potential, x is the distance from the electrode edge and κ is the reciprocal of the Debye length, which is a function of the ionic strength of a solution. The equation shows that potential drops across the double layer strongly dependent on the frequency of applied electric field and conductivities of the medium.

2.3.2 AC Electroosmosis

When an electric field is applied tangential to a surface bathed in electrolyte, the charges in the double layer between the surface and the electrolyte experience a force. Consequently, movement of double layer charges pulls the fluid along the surface and generates a flow, called the AC electroosmosis fluid flow [23]. The time average fluid velocity is given by:

$$v_{ac.omosis} = \frac{1}{8}\frac{\varepsilon_m \phi_o^2 \Omega^2}{\eta x(1+\Omega^2)^2} \qquad (8)$$

where ϕ_o is the applied potential, η is the viscosity of medium and

$$\Omega = \frac{1}{2}\pi\kappa x(\varepsilon_m/\sigma)\omega \qquad (9)$$

The equation shows that the time average fluid velocity strongly depends on both the frequency of applied electric field and the conductivity of the solution.

2.4 Electrothermal Body Force

Electrothermal force is induced because a large power density is generated in the fluid surrounding the electrode when a high electric field is used to manipulate small particles [23]. The electrothermal body force on the fluid is given by:

$$< f_e >= \frac{2}{\pi^3 k}\frac{\sigma V_{rms}^4}{r^2}\prod(1-\frac{2\theta}{\pi})\hat{\theta} \qquad (10)$$

where:

$$\prod = \left[\frac{\alpha-\beta}{1+(\omega\tau_q)^2} - \frac{\alpha}{2}\right] \qquad (11)$$

where V_{rms} is the RMS of applied potential, k is thermal conductivity of the medium, $\alpha = (1/\varepsilon)(\partial\varepsilon/\partial T)$, $\beta = (1/\sigma)(\partial\sigma/\partial T)$ and τ_q is the charge relaxation time (ε/σ). θ and r are defined in Figure 5.

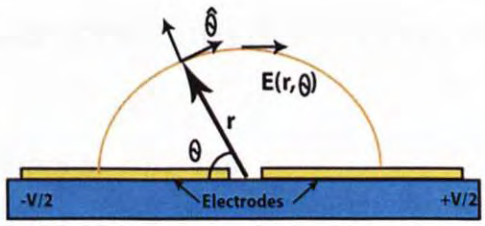

Figure 5 Definition of the parameters θ and r in the electrothermal body force equation [32]

The order of magnitude for a typical fluid flow velocity can be calculated by:

$$|u| = |f_e| \frac{l_o^2}{\eta} \qquad (12)$$

where l_o is the distance characterizing the microelectrode [23].

3. Theoretical Analysis of DEP Manipulation

3.1 Particle Manipulation by DEP Force

Dielectrophoresis (DEP) is defined as the lateral motion generated on uncharged particles due to polarization induced by non-uniform electric fields [22]. The magnitude and direction of dielectrophoresis force are governed by the magnitudes of the applied electric field intensity, freqency, physical dimensions of the NPs, and the real part of the Clausius–Mossotti (CM) factor, respectively. The electric field intensity is determined by both the applied voltage and geometry of the electrodes. The former factor is proportional to the magnitude of DEP force and the latter factor determines the formation position of the NP chains. The simulation of the electric field around the microelectrode used for fabricating AuNP based sensors was performed by Mr. Li Minglin and is shown in Figure 6. The frequency of the input AC signal governs the CM factor which determines the direction of particle movements. The real component of the CM factor of 10nm and 100nm AuNPs suspended in D.I. water is illustrated in Figure 7.

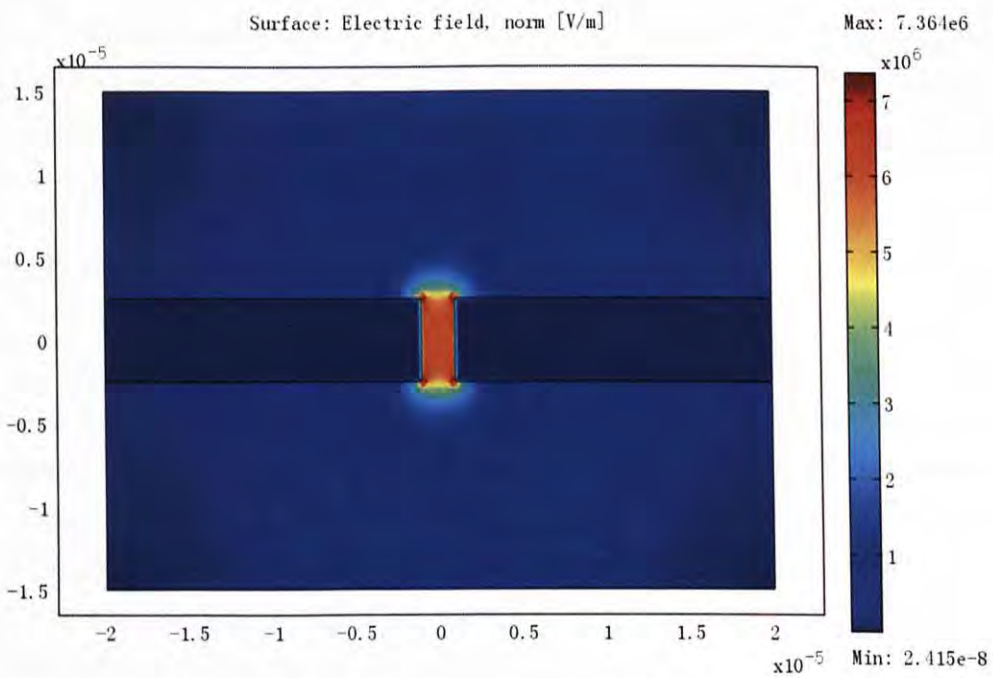

Figure 6 Simulation of the electric field between the electrodes

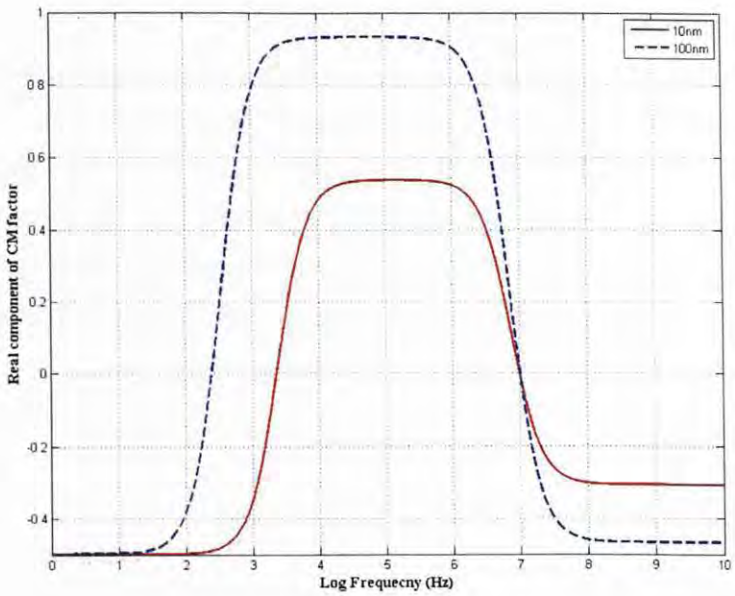

Figure 7 The real part of CM factor for gold colloidal particles with 10nm and 100nm diameters suspended in D.I. water

When the real part of the CM factor is positive, the nanoparticles move towards the strong electric field region and positive DEP force is generated. Once a NP reaches the electrode, it will share the same potential as the electrode and thus the electric field intensity is modified to be higher at its free end. Other NPs in the bulk will move towards the free end (the high electric field region). Eventually, NP chains will form across the electrode gap.

3.2 Electric Induced Fluid Flow

In our experiment on nanoparticle manipulation, AuNPs are dispersed inside a liquid medium. Fluid flow, which is induced by electrothermal force and AC electroosmosis, is imparted on the manipulation process and influenced the particle movements. As mentioned in section 2.2.1, the permittivity of the gold nanoparticles is affected by its single shell structure. Nevertheless, the permittivity of particles does not influence the simulation of AC electrosmosis and electrothermal force; detail may refer to equation (7-12). Therefore, the influence of particle structure on fluid flow can be eliminated.

3.2.1 Double Layer and AC Electroosmosis

AC electroosmosis is induced by the double layer charges, which pulls the fluid along the surface and generates a flow opposite the DEP manipulation. According to equation (7), the

fluid flow velocity strongly depends on both the frequency of applied electric field and the conductivity of the solution. A simulation of the average fluid velocity generated by AC electroosmosis at the middle of the electrode gap is illustrated in Figure 8 as a function of input electric current frequency. We assume that the gold colloidal is suspended in water with the medium conductivity varying from 0.05 to 0.0000055Sm^{-1} and the ionic strength is 0.0006mol dm^{-3} at 25°C. The simulation result concludes that AC electroosmosis induces fluid flow in the low field frequency range only. When the conductivities of the solution increase, the maximum fluid velocity appears in the higher frequency region.

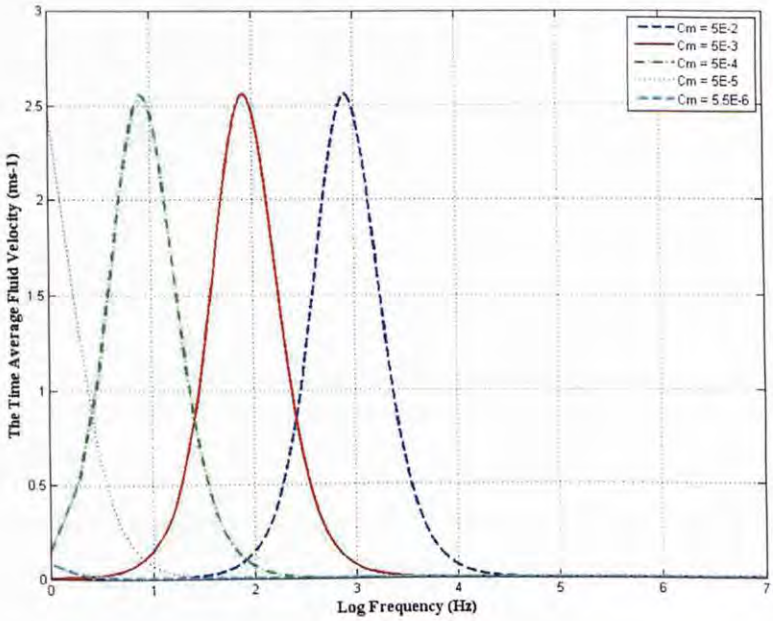

Figure 8 The time averaged fluid velocity by AC electroosmosis at the middle of the electrode gap as a function of frequency at different medium conductivities

Besides the AC electroosmosis effect, the double layer also decreases the magnitude of DEP force. The double layer, induced by electrostatic potential, attracts ions of opposite charge from solution and repels ions with like charge. Eventually, the potential across the electrolyte is less than the input value since the applied voltage drops across the double layer. Thus, the magnitude of DEP force for manipulating the NPs decreases. The amount of voltage drop across the double layer strongly depends on the frequency of the applied current and conductivities of the medium [30][31]. Figure 9 illustrates the potential drops across the double layer for various frequencies for gold colloidal suspended in water with an ionic strength of 0.0006mol dm^{-3} at 25°C. In this simulation, the medium dielectric constant and input voltage is assumed to be $80\varepsilon_o$ and $12V_{pk\text{-}pk}$ respectively. From the result we observe

that potential drop across the electrolyte in the low frequency range only. As under high frequency alternating current, there is insufficient time for the formation of surface charge and a double layer cannot be formed. Another observation is that the frequency range with potential drop across the double layer is wider when the medium conductivity increases.

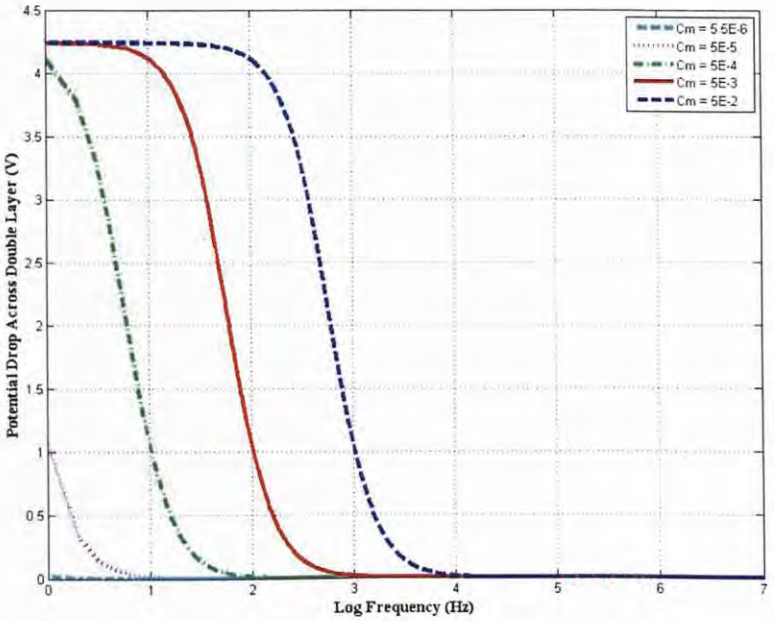

Figure 9 Potential drops across the double layer as a function of frequency at different medium conductivities

3.2.2 Electrothermal Body Force

The heat generated by electric potential induces electrothermal force. Calculation of the order of magnitude of the maximum fluid velocity (θ equal to 0 or π) generated by joule heating under different assumed medium conductivities is shown in Table I. The magnitude of the induced fluid flow velocity is proportional to the medium conductivities. When the conductivity of the medium is high, the power generated per unit volume increases. The applied field frequency determines the direction of the flow. The ratio of electrothermal fluid velocity induced by low and high frequencies is approximately 10:1[23]. When the frequency of the applied signal is smaller than the charge relaxation frequency, fluid flows away from the inter-electrode gap and competes with the DEP manipulation. The opposite situation occurs when the applied signal is higher than the relaxation frequency. Fluid flows towards the inner-electrode gap, which enhances the DEP manipulation. The details are illustrated in Figure 10.

Table 1 Calculation of the order of magnitude of the maximum fluid flow velocity generated by electrothermal body force for gold nanoparticles suspended in water

(Assuming V_{rms}= 8.487, ε_m=80ε, l_o=2μm and η=0.00089 Pa•s. For water, α = -0.4% per degree and β = +2% per degree.)

Solvent Conductivity (Sm^{-1})	**Charge Relaxation frequency τ_q (s^{-1})**	**Order of magnitude of the fluid flow velocity (Note: "-" indicates movement away from electrodes)**	
		Frequency < τ_q	*Frequency* > τ_q
5.5×10^{-6}	7.76×10^{3}	-10^{-5}	10^{-6}
5.0×10^{-5}	7.06×10^{4}	-10^{-4}	10^{-5}
5.0×10^{-4}	7.06×10^{5}	-10^{-3}	10^{-4}
5.0×10^{-3}	7.06×10^{6}	-10^{-2}	10^{-3}
5.0×10^{-2}	7.06×10^{7}	-10^{-1}	10^{-2}

Figure 10 Illustration of fluid flow direction for "+/-" sign indicated in table I

3.3 DEP Manipulation against Fluid Flow

Electric field not only induces DEP force, but also AC electroosmosis and electrothermal force. All the forces take part in the particle manipulation process. During DEP manipulation, DEP force serves as the dominant force whereas AC electrokinetic forces work in different ways, either opposing or enhancing DEP manipulation. In the low frequency region, fluid flow induced by both AC electroosmosis and electrothermal force work against DEP manipulation. When the applied frequency becomes higher, the effect of AC electroosmosis minimizes. Once the applied frequency is higher than the charge relaxation frequency of electrothermal force, the induced fluid flow works in the same direction as the DEP force. Eventually, the fluid motion enhances the DEP manipulation process.

(a) 10nm AuNPs, assuming V_{rms} = 11.314V , σ_m = $5.0\times10^{-5}Sm^{-1}$

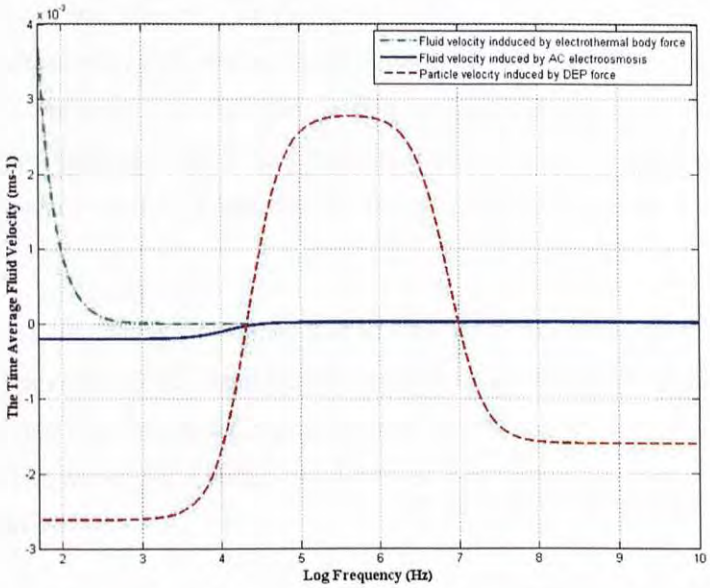

(b) 100nm AuNPs, assuming V_{rms}= 11.314V , σ_m=$5.0\times10^{-5}Sm^{-1}$

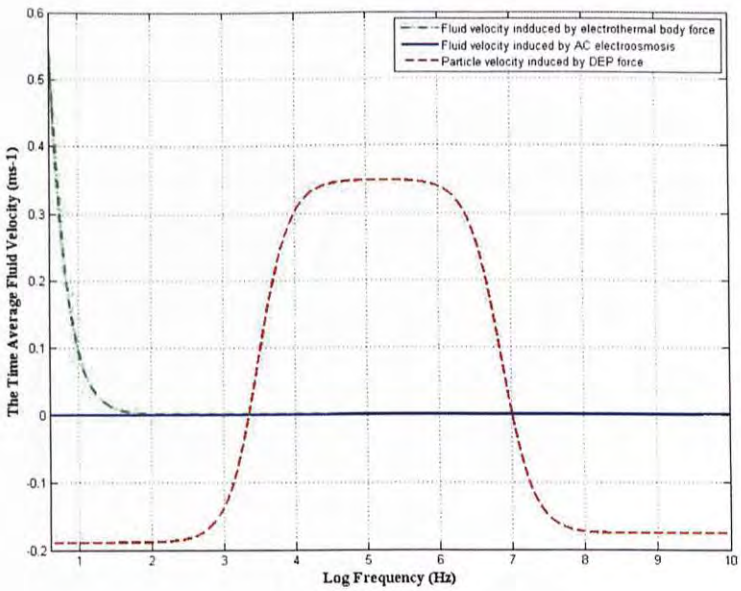

Figure 11 Comparison of the particle velocity against the fluid flow velocity in between the electrode gap for (a) 10nm and (b) 100nm AuNPs suspended in water with medium conductivity equal to $0.00005Sm^{-1}$

(Assuming $\varepsilon_m=80\varepsilon$, $l_o=2\mu m$, $\eta=0.00089$ Pa•s, $\chi=0.7\mu m$, $r=0.5\mu m$, $\theta=45°$, and the ionic strength is 0.0006mol dm^{-3} at 25°C. For water, α and β is ≈ -0.4% per degree and +2% per degree.)

Figure 11 compares the time average particle velocity generated by DEP force with the fluid velocity induced by AC electokinetic force in between the electrodes. The simulation results show that under specific frequency range, particle velocity induced by DEP force is higher than the fluid velocities. AuNPs are manipulated by DEP force and a pearl chain is formed across the microelectrodes. For example, in plot (a), particle velocity generated by DEP force is higher than the fluid flow velocities in the frequency range from 40k to 1MHz. Thus, under this frequency range, 10nm AuNP based pearl chains can form across the microelectrodes.

Plot (b) shows the simulation for 100nm AuNPs. The DEP force is larger than other forces except for the frequency of the input current is lower than 1Hz. In conclusion, the results show that the 10nm AuNPs can be manipulated by DEP force when the frequency ranges from 40k to 1MHz, whereas the 100nm Au NP based pearl chain can form in the frequency range 5k to 500kHz.

In the above simulation, the real part of the CM factor of 10nm and 100nm AuNPs is simulated based on the experimental result shown in Figure 24(ii). The simulated CM factor is plotted in Figure 12. We assumed that the thickness of the shell is 2nm, and the dielectric constant of the core sphere, shell and medium are $70\varepsilon_o$, $1\varepsilon_o$ and $80\varepsilon_o$ respectively, whereas the conductivity of the core sphere, shell and medium are assumed to be $1\times10^{-6}Sm^{-1}$, $1\times10^{-2}Sm^{-1}$ and $5\times10^{-5}Sm^{-1}$.

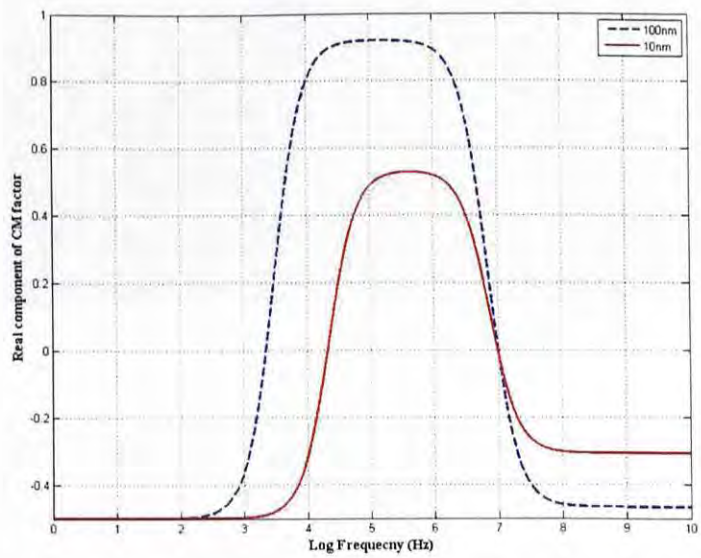

Figure 12 The simulated Re[CM] of 10nm and 100nm AuNPs suspended in water with medium conductivity equal to $0.00005Sm^{-1}$

4. Fabrication of AuNP based Sensors

The fabrication process of a gold nano-particle based sensor is separated into three parts, which include fabrication of gold microelectrodes, formation of the gold pearl chain across the microelectrodes and packaging of the sensor chips onto a PCB board. After the microelectrodes are fabricated, AuNPs are manipulated to align across the microelectrodes by DEP force to achieve the pearl chain structure, which works as a sensing element of the sensor. Finally, the chip is packed onto a PCB board by sliver epoxy or wire bonding, so that the sensor can connect to other electrical components or devices for further application.

4.1 Fabrication of Arrays of Microelectrodes

Au microelectrodes with a gap separation of 2μm (Figure 13) were fabricated on Si/SiO2 substrates by a lift-off process. Si wafers were first cleaned by immersing them in acetone, followed by IPA and finally in DI-water. Then photoresist (AZ5214E) was spin-coated onto the wafers at 3,000rpm. The photoresist was then patterned by negative lithography. Finally, layers of 500Å chromium and 3000Å gold films were deposited on top of the patterned photoresist by electron beam evaporation before lift-off. The fabrication process is listed in Figure 14.

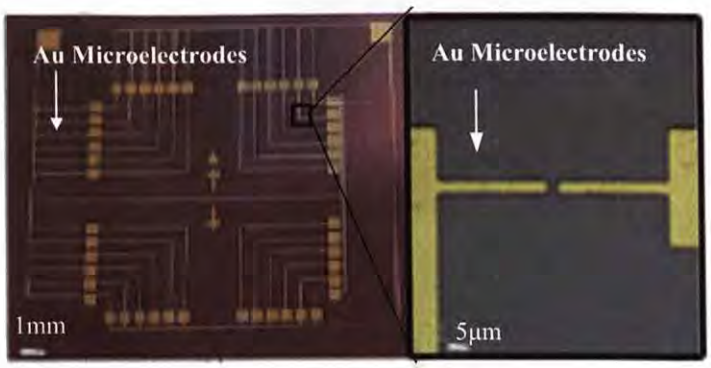

(a) (b)

Figure 13 (a) Micro-photograph of Au microelectrodes fabricated on a Si substrate. (b) Optical image showing a pair of microelectrodes

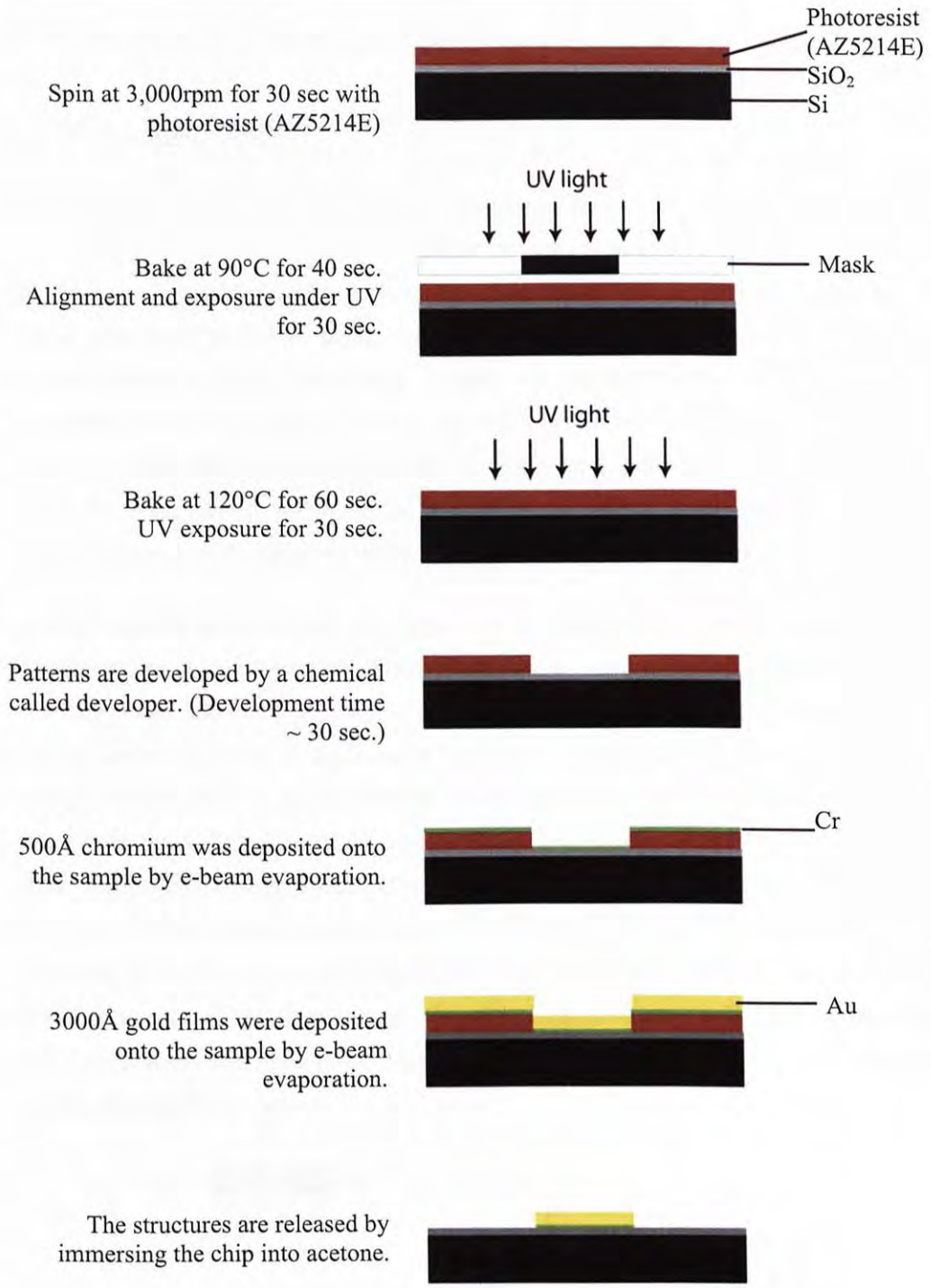

Figure 14 Fabrication process of the gold microelectrodes

4.2 Formation of AuNP based Pearl Chains across Microelectrodes

4.2.1 Formation Circuit

The experimental setup was developed as shown in Figure 15. A pulse/Function Generator (Hp 811A, Hewlett Packard Company, USA) was used to generate a sinusoidal A.C. current input for pearl chain formation. A digital Real-Time Oscilloscope (TDS 220, Tektronix, Inc. USA) measured both the input voltage (CH 1) and voltage passing through the microelectrodes (CH 2). The voltage passing through Resistor A can be calculated by subtracting the voltage passing through the microelectrodes (CH1 – CH2) from the input voltage. A stopwatch recorded the duration of gold pearl chain formation, thus the time in between voltage change was observed using the oscilloscope. A resistor was connected in series to prevent overheating and undesired growth of the Au pearl chain.

Before the pearl chain formed, the circuit can be considered an open circuit with infinite resistance, since the microelectrodes are unconnected. Voltages drop across the microelectrodes and Resistor A before and after the PCF were measured by the oscilloscope. At the beginning, most of the voltage is drawn by the microelectrodes. When $12V_{pk\text{-}pk}$ voltages were applied to the circuit, the voltage across the microelectrodes and Resistor A were measured around $100mV_{pk\text{-}pk}$ and $11.9V_{pk\text{-}pk}$ respectively. After the PCF, the resistor draws most of the voltage. Figure 16 shows both the measured and theoretically calculated (by Ohm's Law) voltages between Resistor A and microelectrodes respectively. The average resistance of the formed Au pearl chain was measured around 102.54Ω with the standard deviation around 13.6Ω. From the experimental result, Resistor A with 3kΩ was chosen, so that the resistor could draw more than 95% of the input voltage when a pearl chain with ~100Ω resistance was formed.

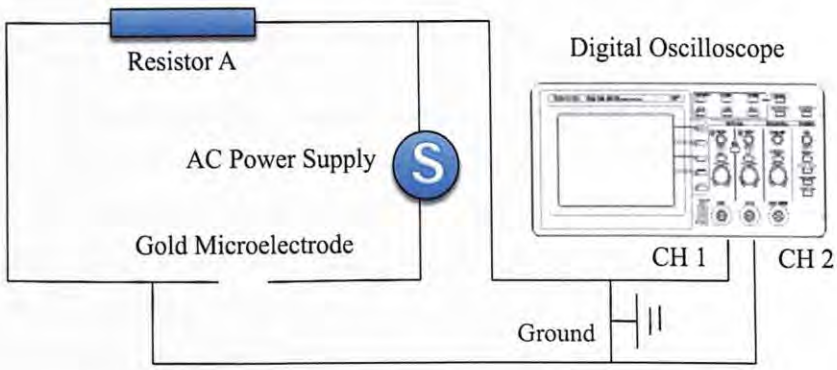

Figure 15 A schematic diagram of the experimental setup for Au pearl chain formation detection

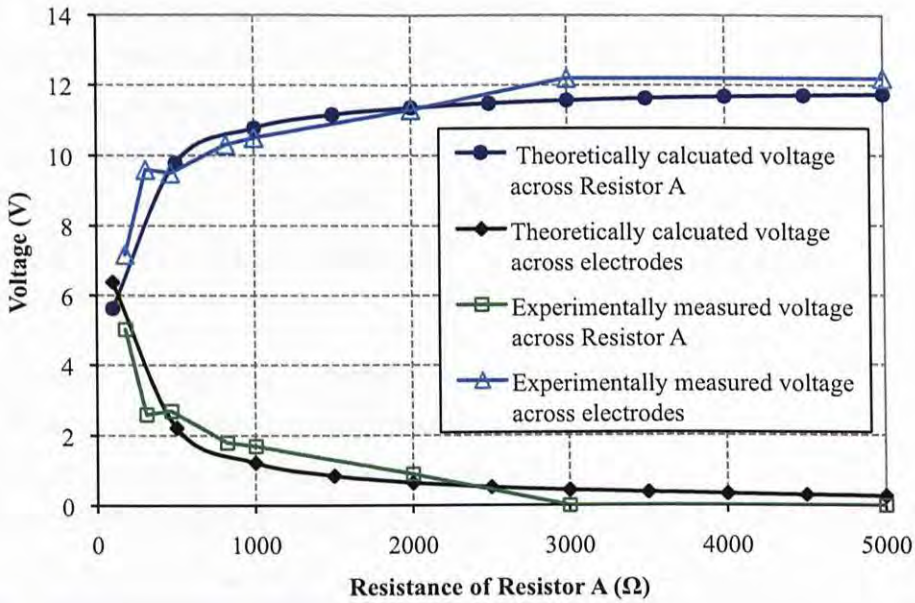

Figure 16 Theoretically calculated and experimentally measured voltages across both the microelectrodes and Resistor A after the PCF when a resistor with various resistances is connected to the circuit

4.2.2 Microspotting System

Our advisor and Dr. King K. C. Lai, the alumni of our group have previously developed a computer-controlled microspotting system [33]. Controlled volumes of solutions can be precisely spotted across the microelectrodes, resulting in a high yield and high precision rapid assembly method for gold nano-particle based sensors. The microspotting system, as shown in Figure 17, is integrated by: a computer controllable X-Y-Z micromanipulator (MP285, Shutter Instrument Company), a computer controllable hydraulic pump (V6 syringe drive modules, Kloehn Limited) and a CCD video camera connected to the microscope. A real-time microscopic image was observed on a computer screen and served as a visual aid for moving the capillary probe tips to the desired position.

During the experiment, a capillary probe with inner diameter of 50μm and outer diameter of 150μm was mounted on the X-Y-Z micromanipulator. After the substrate with the microelectrodes was placed onto the stage, the X-Y-Z micromanipulator moved the probe to an appropriate position. A syringe pump connected to the probe then injected the solution droplet onto the substrate. A typical single droplet contact injection process was used in our experiment. Initially, the probe tip was moved to 30μm above the substrate. A pressure was applied to the probe through the syringe pump, and then a concave-shaped solution was formed at the probe tip due to the surface tension and the droplet size was kept increasing.

Once the solution touched the substrate, it was in contact with both the probe tip and substrate. The probe-solution-substrate connection was stable if the probe tip remained stationary and no external force was applied. When the probe was moved upwards, the connection was broken and a droplet of solution with radius ~250μm was dropped onto the substrate. The finest spot size can be achieved by our microspotting system is around 40μm, however, the solution droplet evaporate before a pearl chain is successfully formed across the microelectrodes if the spot size is too small. PCF is prohibited by solvent evaporation.

To perform microspotting on a substrate with microelectrodes, we can input the positions of the microelectrodes manually or automatically by loading the CIF-mask file into the control program of the system. After aligning the initial position of the microelectrodes, the probe tip can be moved sequentially to positions above each microelectrode and spotted on them.

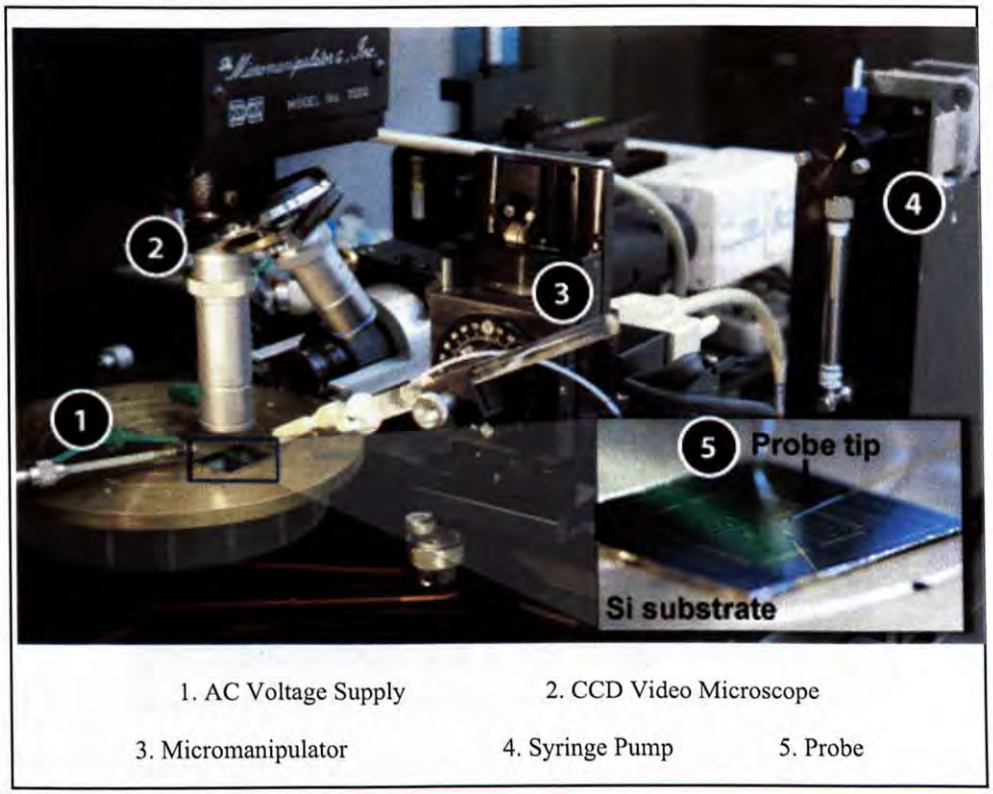

Figure 17 The microspotting system with CCD video, micromanipulator and syringe pump

4.2.3 Results and Discussion

A controlled volume of gold colloidal solution (EM, GC series from British Biocell International, Cardiff, UK) with a diameter of 10nm and 100nm particles were precisely spotted across the microelectrodes using the single droplet contact injection method using the microspotting system. The Au microelectrodes were excited by an AC voltage of

typically $14V_{pk-pk}$ with a frequency of 50kHz for 100nm AuNPs or 100kHz for 10nm AuNPs. DEP force was induced across the microelectrodes and the gold pearl chain was formed. Figure 18 and Figure 19 show the timeline of Au PCF and the SEM images of the Au pearl chain formed by 10nm AuNPs and 100nm AuNPs.

Generally, the Au pearl chains form across the microelectrodes in a few minutes under optimum conditions. From the SEM images of the Au pearl chain formed by 100nm AuNPs, we can clearly observe that the spherical particles are linked together one by one. Due to the heat induced by the external electric field, some of the particles melt and accumulate together. A large structure is formed in between the particles and the original spherical shape is deformed.

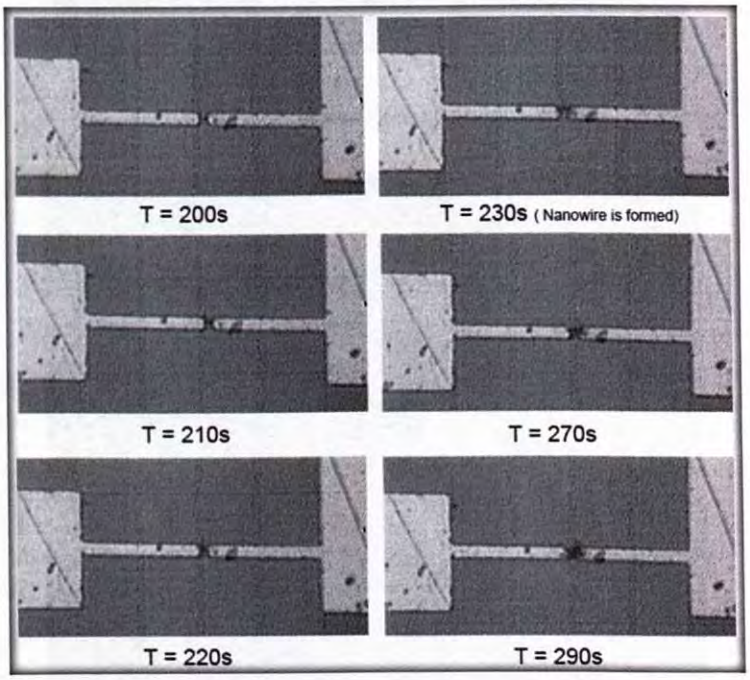

Figure 18 Timeline of the Au PCF under positive DEP force. (Before T=200s, an almost blank microelectrode gap was observed. Only a few nanoparticles were attached on both microelectrodes.)

(a) Gold Pearl Chains from by 10nm AuNPs

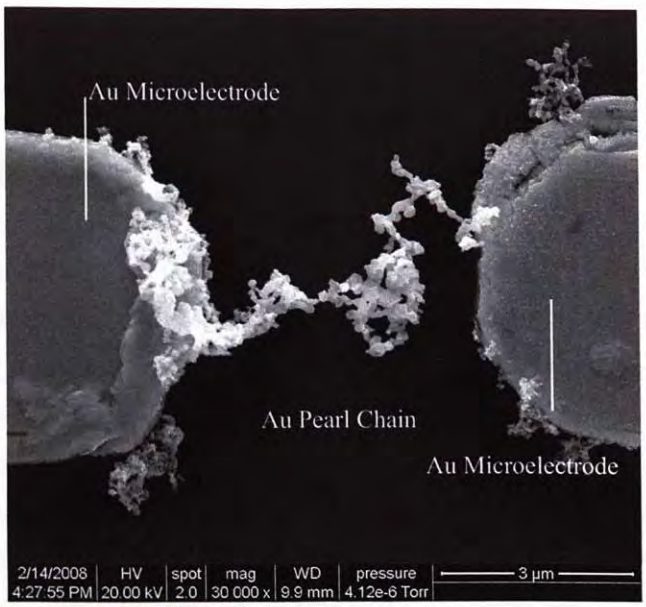

(b) Gold Pearl Chains from by 100nm AuNPs

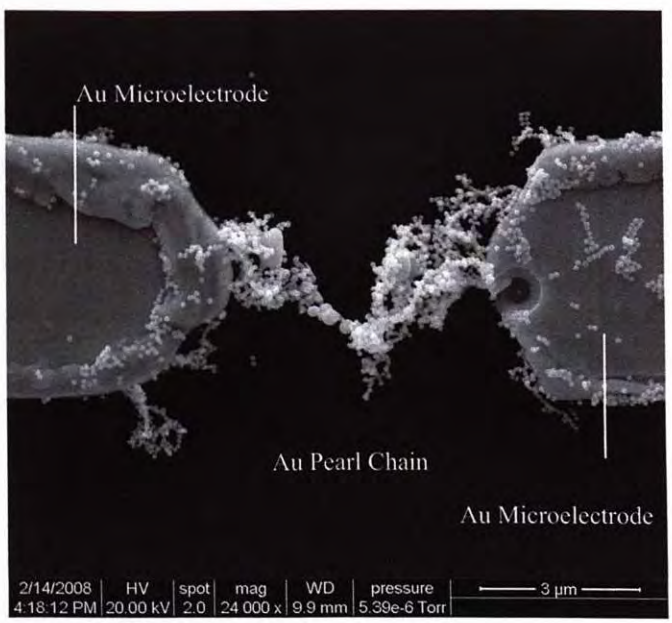

Figure 19 SEM images of the gold pearl chain formed by (a) 10nm AuNPs and (b) 100nm AuNPs

5. Exploring the Critical Parameters in Controlling AuNP Pearl Chain Formation (PCF)

5.1 Exploring the Optimum Frequencies

According to the theories of DEP, the real part of the Clausius-Mossotti (CM) factor determines the direction of dipoles. Particles move towards a strong field region when the factor is positive and positive DEP force is induced. The opposite situation occurs for negative DEP. Based on the experimental result of the PCF rate under 12 $V_{pk\text{-}pk}$, the CM factor of 10nm and 100nm AuNPs is theoretically simulated using the single shell model sphere and plotted in Figure 20. It is apparent that DEP force dominates when frequency is higher than 40kHz and 5kHz when the particle size is equal to 10nm and 100nm respectively. Below those frequencies, electrolysis and electroosmosis effects dominate, which prohibit the PCF of NPs.

For the frequency ranges with negative CM factor (e.g. below 5kHz and above 1MHz in 100nm AuNPs), experimentally almost no pearl chain formation was observed. Since particles experienced negative DEP force and were repelled from the electrodes, fluid flow induced by AC electroosmosis and electrothermal force caused the non-uniform distributions of gold particles in the solution. From low to high frequencies, the dominant fluid flow shifts from the AC electroosmotic flow to electrothermal flow. The magnitude of the AC electroosmotic flow decreases when frequency increases whereas the electrothermal flow is generated under all frequency ranges. Further studies on the dominant forces under specific frequency ranges will be explained in the next section.

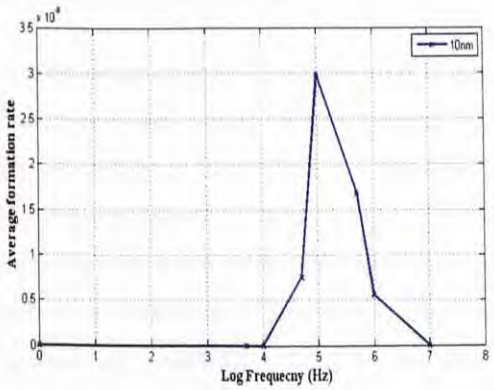

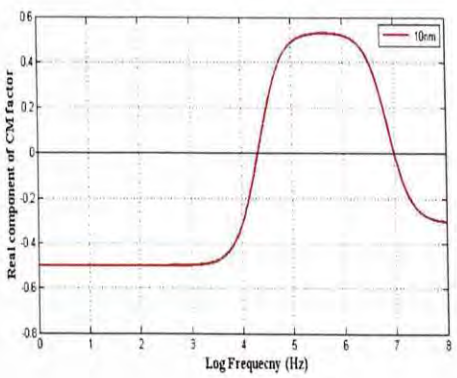

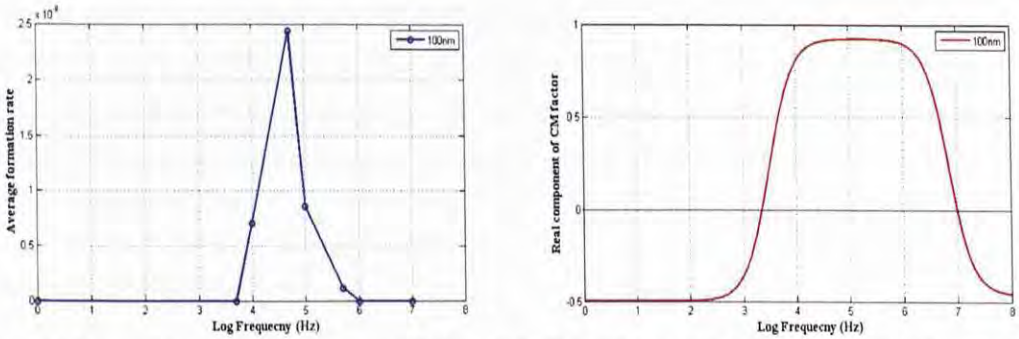

Figure 20 Comparsion of the experimental PCF with the theoretical calculated CM factor of 10nm and 100nm single shell model sphere. It is apparent that DEP force dominates when frequency is higher than 5kHz and 40kHz when the particle size is equal to 100nm and 10nm respectively.

5.1.1 Analyzing the observation of pearl chain formation under specific frequency ranges

(A) From 10Hz to 100Hz

When the applied frequency is lower than 100Hz, formation of bubbles caused by AC electrolysis prohibits PCF. Hydrogen and oxygen gas bubbles are generated due to the electrolysis of water. The minimum voltage input for electrolysis of water is 1.23V for DI water, which is determined by the Nernst equation (the detail is shown in Appendix II). However, the actual voltage to cause electrolysis is higher, which depends on the ion concentration and electrode gap distance. In our experiment, bubbles started to form at $2.3V_{rms}$ under 25Hz frequency. The rate of bubble growth increased with the applied voltage. The amount of bubbles generated decreased when the frequency increased, as redox reactions are limited by high frequency AC signals.

(B) From 100Hz to 10kHz

According to Figure 12, negative DEP force is induced and particles are repelled from the microelectrodes under this frequency range (except for 100nm AuNPs with applied frequency higher than ~5kHz). Therefore, no pearl chain formation was observed. Besides the dielectrophoresis effect, the AC electroosmosis and double layer effects influence the movement of the AuNPs. AC electroosmosis induces fluid flow, which works against DEP particle manipulation. The order of magnitude of the maximum fluid velocity generated by the AC electroosmosis effect is in the order of 10^{-1}, whereas the particle velocities generated by DEP force for 10nm and 100nm AuNPs are calculated in the order of 10^{-3} and 10^{-1} respectively as shown in Figure 11. For AuNPs with diameters smaller than 100nm, the fluid

velocity is approximately 10 times higher than the particle velocity generated by the DEP force. Moreover the magnitude of DEP force decreases as the double layer draws most of the input potential. In conclusion, the AC electroosmosis effect is the dominant effect in most cases under the low frequency range. As the AuNPs are freely suspended in the solution and the fluid flow induces a pushing force which acts on the AuNPs, particles move along with the fluid motion.

(C) 10kHz for 10nm Au NPs

When an alternating current at 10kHz is applied to the circuit, positive DEP force is induced. Ideally, AuNPs are manipulated by the DEP force and aligned across the microelectrodes. However, Figure 21 shows that the pearl chain was formed away from the inter-electrode gap. This can be explained by the theory of electrothermal body force. The direction of the electrothermal induced fluid flow is determined by the charge relaxation frequency of the suspending medium. When the frequency of applied signal is smaller than the charge relaxation frequency, $\prod$ factor is negative (refer to (10)) and fluid flows away from the inter-electrode gap [31]. When the $\prod$ factor is positive, fluid flows towards the inter-electrode gap. According to Table I, the charge relaxation frequency is around 10kHz when the medium conductivity is between 5.5×10^{-6} and 5.0×10^{-5} Sm^{-1}. In our experiment, AuNPs are suspended in D.I. water. The medium conductivity of pure D.I. water is around 5.5×10^{-6} Sm^{-1}. However, the manufacturer claimed that chemical residual is left from manufacturing and chloride ion is presented in the colloidal solution. Thus, the actual medium conductivity of the gold solution is potentially in the range of 5.5×10^{-6} to 5.0×10^{-5} Sm^{-1}. Therefore, we can conclude that pearl chains form away from the microelectrode because of the influence of the fluid flow induced by electrothermal force.

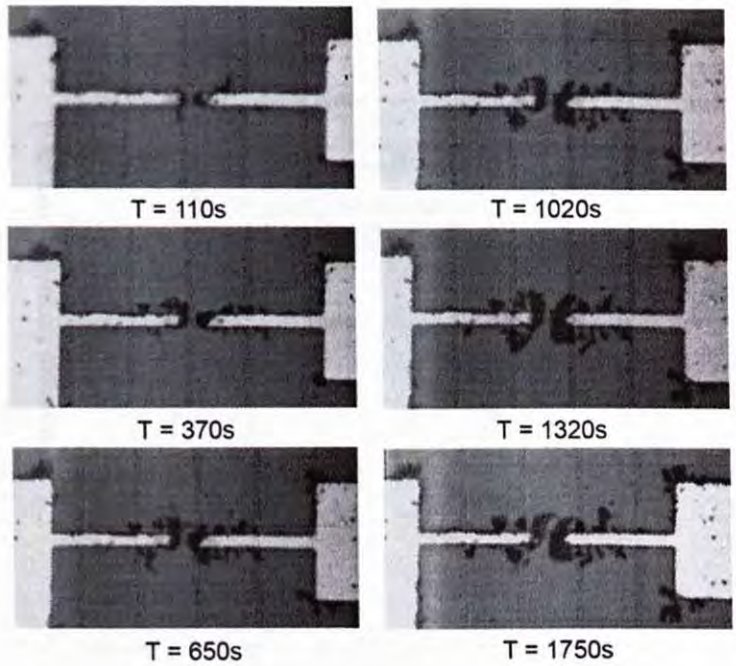

Figure 21 Timeline of Au pearl chains forming away from the inter-electrode gap

(D) 10kHz to 5MHz for 100nm AuNPs, 10kHz to 10MHz for 10nm AuNPs

In this specific frequency range, positive DEP force is induced and works as the dominant force to manipulate the AuNPs. The nanoparticles move towards a high electric field region and an Au NP based pearl chain forms across the microelectrodes. Variations in formation rate were detected when the applied voltage and the particle size varied. Experimental results in Figure 22 show that the formation rate increases when the input voltage increases since the magnitude of DEP force is proportional to ∇E_{rms}^2. More details will be presented in section 5.2. On the other hand, when the particle size decreased, the applied frequency level for achieving the optimum formation rate shifted to the higher frequency region. The experimental result is shown in Figure 23. Besides the variation in optimum frequency level, the formation rate also varies with the particle size. Theoretical calculation shows that the particle velocity induced by DEP force on 100nm particles is 100 times faster than that on 10nm particles. However, our experimental results show that 10nm particles form a 2μm pearl chain faster or in about the same time as 100nm particles. Detailed explanations will be given in Section 5.3.

(i)

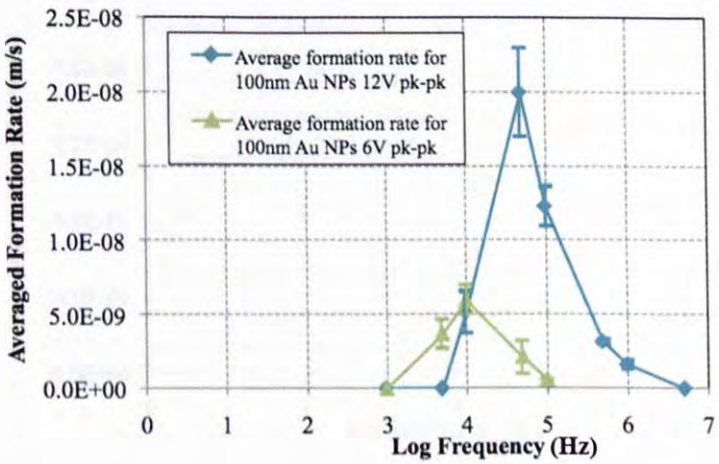

(ii)

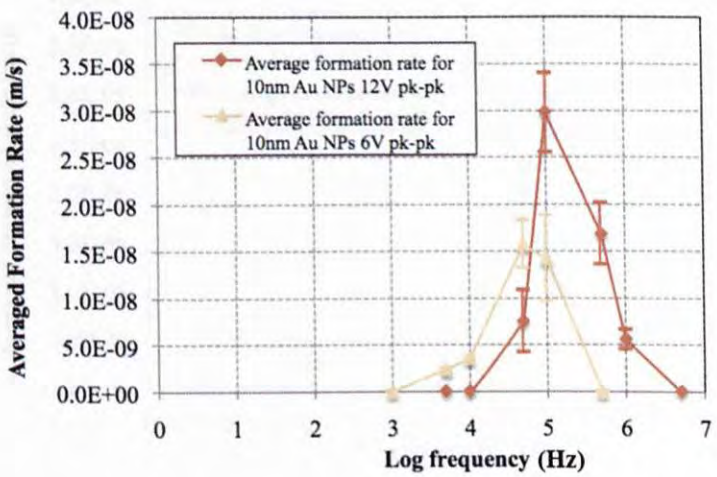

Figure 22 Experimental results of PCF rate of (i) 100nm under 6 V_{pk-pk} and 12 V_{pk-pk}; (ii) 10nm under 6 V_{pk-pk} and V_{pk-pk}.

(i)

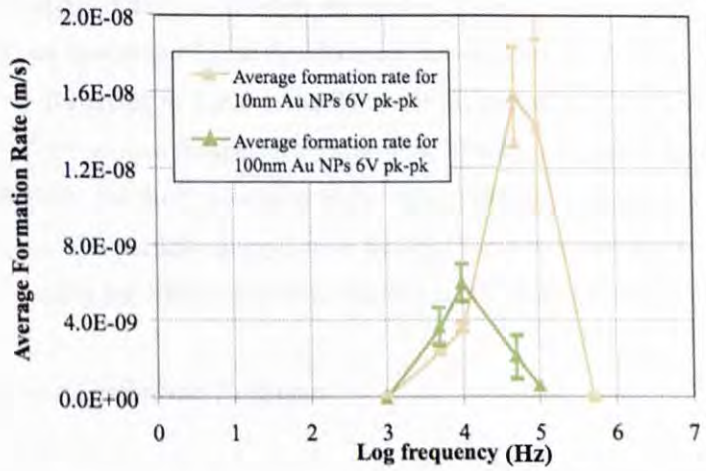

(ii)

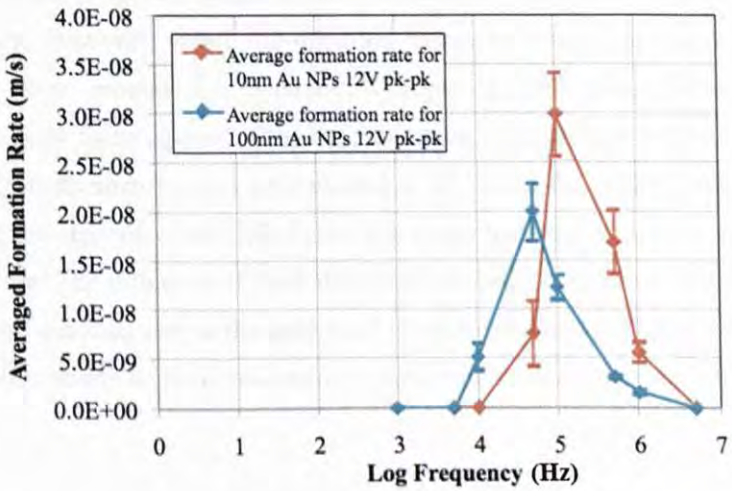

Figure 23 Experimental results of PCF rate of (i) 10nm and 100nm under 6 V_{pk-pk} (ii) 10nm and 100nm under 12 V_{pk-pk}

5.1.2 Conclusion on the Optimum Frequency for PCF

The direction of the dielectrophoresis force is determined by the real part of the CM factor, which is governed by the applied frequency. Pearl chains can be sucessfully formed across the microelectrodes when the CM factor is positive. Besides the direction of DEP force, the applied frequency also determines the direction and magnitude of fluid flow. Under the low frequency range, both AC electroosmosis and electrothermal body force induce fluid flow which moves away from the electrode and works against the PCF manipulated by DEP force. The maximum fluid velocity induced by AC electroosmosis is in the order of 10^{-1} whereas the particle velocity induced by DEP force is in the order of 10^{-3} and 10^{-1} for 10nm and 100nm AuNPs respectively. In our experiment, the magnitude of fluid velocity induced

by AC electroosmosis reached a maximum when the applied frequency was equal to 1Hz and minimized to approximatly zero when the applied frequecy was higher than 100Hz. In Section 5.1.1(C), we investigated that the electrical conductivity of the colloidal solution is ~$5.0\times10^{-5}Sm^{-1}$[34]. Referring to Table 1, the fluid velocity induced by electrothermal force is in the order of 10^{-4} for applied frequencies lower than 70.6kHz. When the applied frequency is higher than 70.6kHz, the fluid velocity is in the order of 10^{-5} in a direction moving towards the microelectrodes. The particle manipulation by DEP force is enhanced by the fluid flow. The optimum frequency for 100nm and 10nm AuNPs is 50kHz and 100kHz respectively.

5.2 Exploring the Optimum Voltages

According to DEP equation (1), the magnitude of DEP force increases with voltage, so a high voltage should be applied to the circuit in order to maximize the formation rate of the gold pearl chain. However, within the optimum frequency range, the electrothermal force induced fluid flow around the electrode. Comparing DEP force equation (1) with electrothermal body force equation (10) the magnitude of DEP force is proportional to V^2 whereas the electrothermal force is proportional to V^4. When the applied voltage increases, the increase of the electrothermal fluid velocity is larger than that of particle velocity driven by the DEP force. The influence of fluid flow becomes more significant under high applied voltage and the formation rate of the gold pearl chain slowed down. Figure 24 estimates the ratio of particle velocity to fluid velocity for 10nm AuNPs under various applied voltages, where:

$$\gamma = \frac{particle\ \ velocity\ \ (v_{DEP})}{fluid\ \ velocity\ \ (v_{Electrothermal})} \qquad (13)$$

The ratio changes from 97.7 to 3.44 when the applied voltage varies from $1V_{pk\text{-}pk}$ to $27V_{pk\text{-}pk}$.

In the case of 100nm AuNPs, the particle velocity generated by DEP force is in the order of 10^{-1}. When applied voltage ranges from $3V_{pk\text{-}pk}$ to $18V_{pk\text{-}pk}$, the particle velocity is at least a hundred times higher than the fluid flow velocity. Experimental results in PCF rate under various applied voltage is shown in Figure 25. In conclusion, the influence of electrothermal force minimizes when the particle size increases and the formation rate is proportional to V^2. Although high voltage can generate a high formation rate, the microelectrodes would melt because of the high temperature caused by the high voltage. From experimental observations, the best voltage for formation is the range from $12V_{pk\text{-}pk}$ to $16V_{pk\text{-}pk}$ in order to maintain high formation rate and prevent melting of microelectrodes.

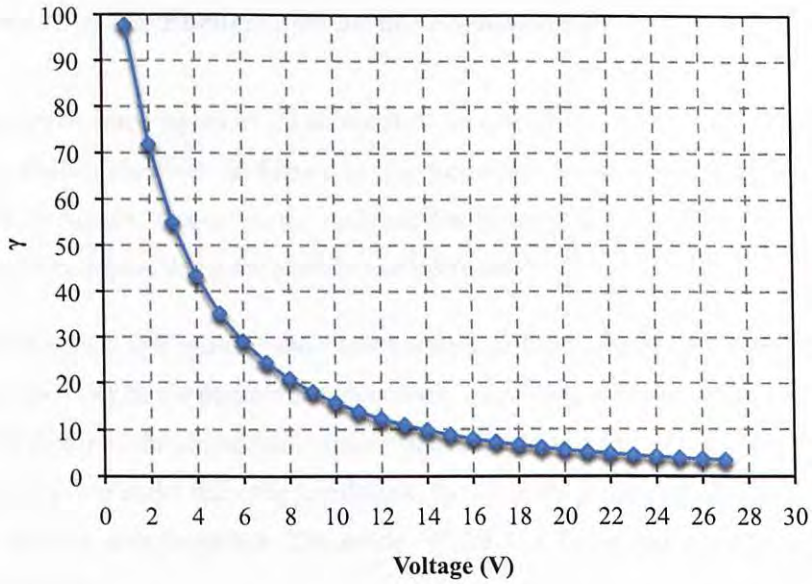

Figure 24 Comparison between the particle velocity generated by DEP force and the fluid velocity generated by electrothermal body force (10nm AuNPs, 100kHz)

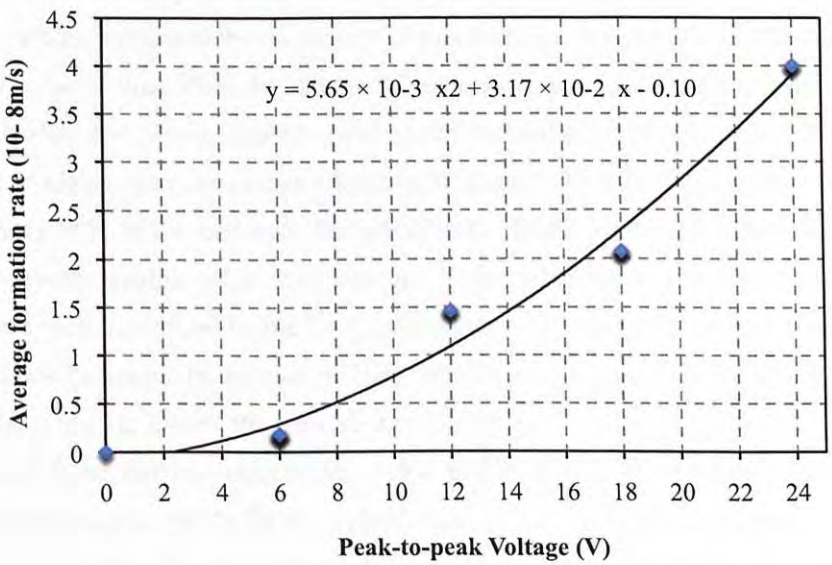

Figure 25 Average formation rates for 100nm AuNPs under various voltages (50kHz)

5.3 Influence of the Particle size on the Formation Rate

Dielectrophoresis force equation (1) shows that the magnitude of DEP force increases with the particle radius. However, in Figure 23, the formation rate of 10nm AuNPs is similar to that of 100nm AuNPs. Moreover, the optimum frequency of the gold NPs PCF shifts to the higher frequency region when the particle size decreases.

Experimental results in Figure 32 show that the optimum frequency of PCF shifts to a higher frequency region when the particle size decreases. According to Figure 42(b) in Appendix-I, the real CM factor of the single shell models shows a similar result. If both 10nm and 100nm AuNPs solution are under the same conditions, the optimum frequency of PCF will increase when the particle size decreases. The model of the CM factor explains the difference in optimum frequency.

On the other hand, the difference in formation rate can be explained by the influence of electrothermal fluid flow. When an electric current is applied across the electrodes, DEP force is induced to manipulate the AuNPs. Besides that, the electrothermal force generates fluid flow, which influences the movement of nanoparticles. From Table 1, when the applied frequency is lower than 70.6kHz (charge relaxation frequency), fluid flows away from the microelectrodes and works against pearl chain formation. However, when the applied frequency is higher than the charge relaxation frequency, fluid flows towards the electrode and enhances PCF. In the first case, the rate of pearl chain formation is slowed down as the fluid flow works against DEP manipulation. In the other case, both the fluid flow and nanoparticle motion induced by the DEP force work in the same direction, so eventually the formation rate increases. In the case of 10nm AuNPs, the optimum frequency for formation is 100kHz, which is higher than the charge relaxation frequency (~70.6 kHz). The fluid flows away from the microelectrode, which prohibits DEP manipulation, whereas the optimum frequency is 50kHz for the 100nm case, where the opposite situation occurs. The fluid flows towards the microelectrode gap, which enhances DEP manipulation. In conclusion, the formation rate of 10nm Au NP based pearl chains is similar to that of 100nm AuNPs.

6. Characteristics of the AuNP based Pearl Chain

6.1 I-V Characteristics

I-V Characteristics of the gold nano-particle based sensor were determined by connecting a source meter (Model 2400 General-Purpose SourceMeter, Keithley, Instruments, Inc.) to the Au pearl chain in series. The results for 10nm and 100nm AuNP based pearl chains are shown in Figure 26 and Figure 27 respectively. They show that the sensor could be operated in ~mW. The measured resistance of the sensors were ~100Ω. Variation of resistance between different sensors was found because of the random connections between nanoparticles during the DEP manipulation process. In spite of the variations, all samples were found to have similar linear I-V characteristics, which obeyed Ohm's Law.

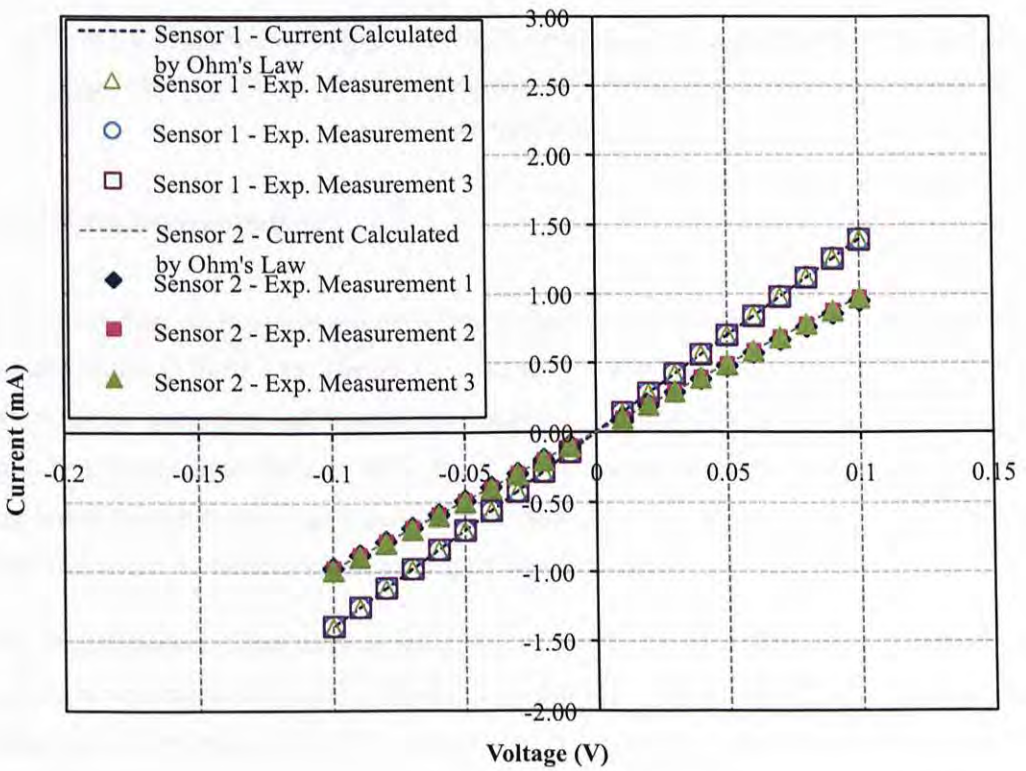

Figure 26 I-V Characteristics of gold nanoparticle chains formed by 10nm AuNPs in the voltage range -0.1V to 0.1V. Three repeated measurements were performed for in sensors to validate the repeatability. The straight line is the theoretical expectation using Ohm's law.

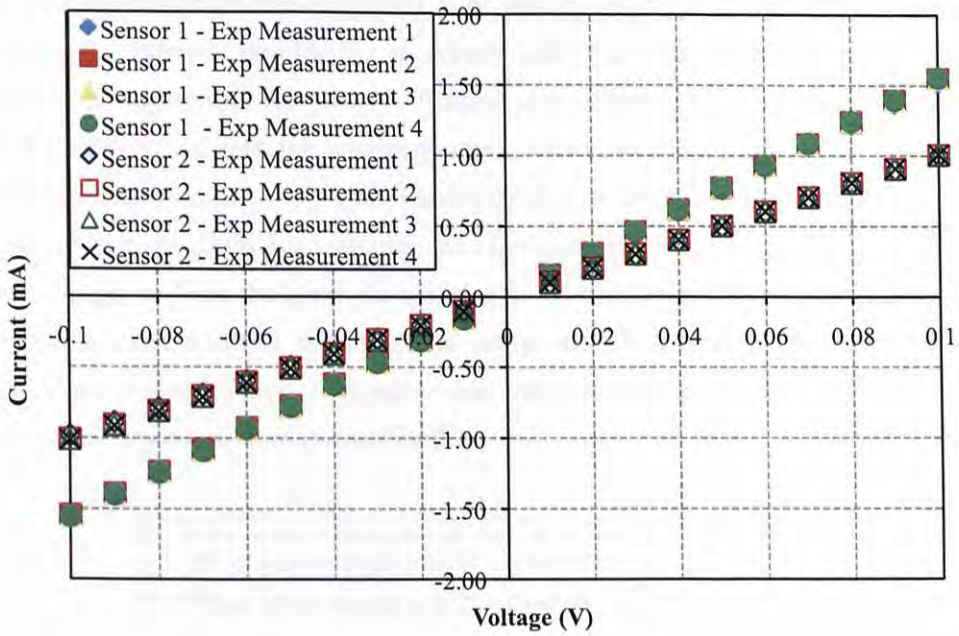

Figure 27 I-V Characteristics of gold nanoparticle chains formed by 100nm AuNPs in the voltage range -0.1V to 0.1V. Four repeated measurements were performed in two sensors to validate the repeatability.

6.2 Thermal Sensitivities

The sensor chip, packaged on a printed circuit board (PCB), was put inside a programmable climate chamber (KBF-115, Binder Co., Germany). The resistance change of the AuNP based sensor was measured against the temperature inside the chamber. A few thermal annealing cycles from 20°C to 80°C for 5 cycles were performed. A representative and repeatable data set is shown in Figure 28. A considerable room temperature resistance drift is observed due to the detachment of some gold nanoparticles.

The TCR determined the thermal sensitivity of the AuNP based sensors. An increase in resistance was measured when the temperature increased, which implied the thermal sensing capability of the sensor. The TCR was obtained by measuring the resistance change of the gold nano-particle based sensor with corresponding temperature and was calculated by:

$$R(T) = R_o(1 + \alpha(T - T_o)) \qquad (14)$$

where R_o is the resistance at room temperature T_o, and α are the temperature coefficients of resistance. The TCR of the sensor was found to be around 0.1%/°C.

A similar experiment to explore the TCR of gold microwire was performed. Figure 29 compares the thermal sensitivities of typical gold, gold microwire and pearl chains. Variations in sensitivities are observed because of their structural and material difference. Different from typical gold, the gold microwire compose of chromium and gold. Structurally gold microwire is similar to the gold microelectrodes, except that a 2μm gap is in between the microelectrode. Gold nanoparticles, which surrounded by chemical stabilizers, align across the gap to form the pearl chain structure. Although the TCR shows that the gold microwire is more sensitive to temperature change than the gold pearl chain, we observed that gold pearl chain is more responsible than the microwire in gas flow detection. Detail experimental results are shown in section 7.2.

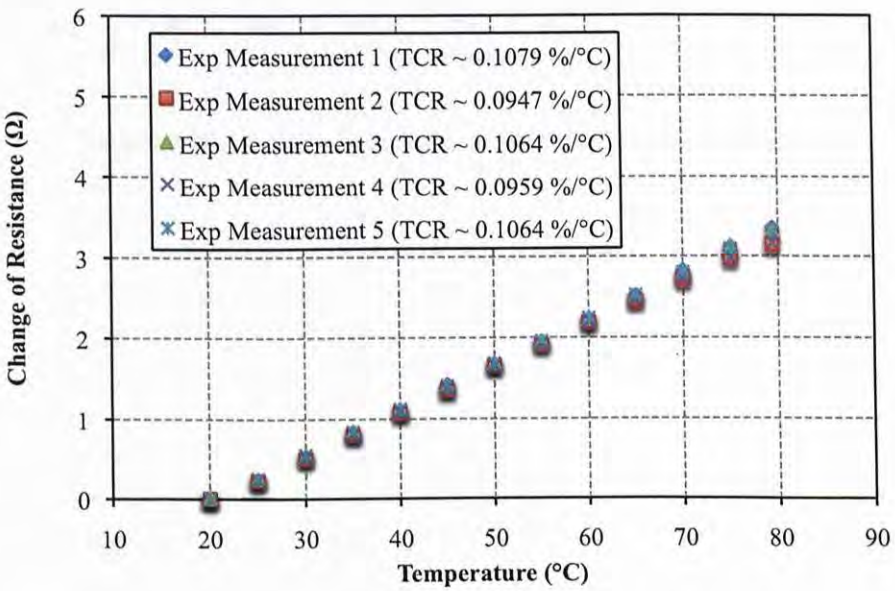

Figure 28 TCR variation of a gold NP based sensor. Five repeated measurements were performed in the same sensor to validate the repeatability.

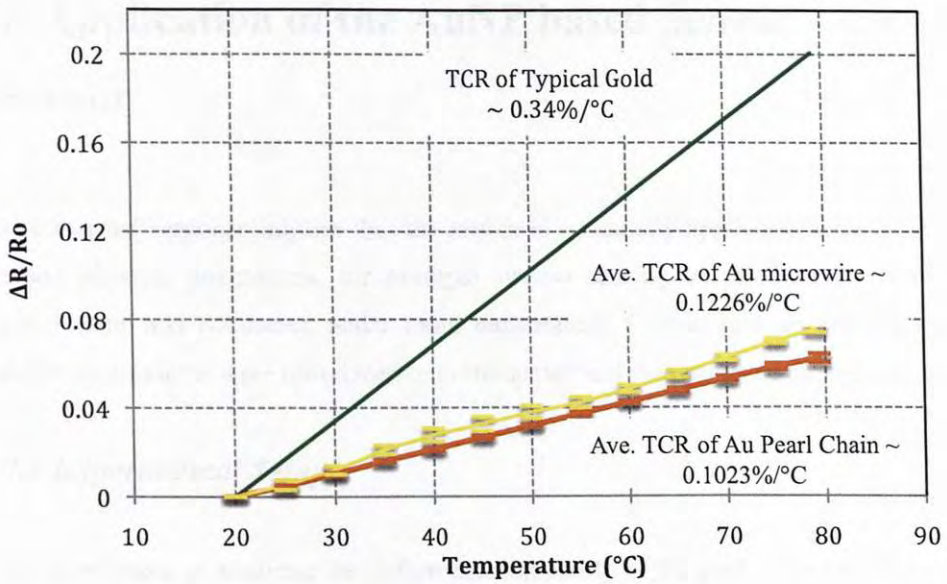

Figure 29 TCR variation of typical gold, gold microwire and pearl chains

7. Application of the AuNP based Sensor – Airflow Sensor

The thermal response implies that the sensor is potentially applied to sense other thermal-based physical phenomena, for example airflow sensing. A preliminary airflow sensing experiment was conducted under room temperature. Compressed air and nitrogen gas at different pressures were introduced onto the sensor and the resistance change was measured.

7.1 Experimental Setup

An experiment on studying the airflow sensing ability of the gold nano-particle based sensor was performed under room temperature. The experimental setup was developed as shown in Figure 30. Compressed air or nitrogen gas at different pressures was introduced onto the sensor through plastic tubing with an inner diameter of 3mm and 348mm in length. The outlet of the plastic tubing was placed on top of the pearl chain with a distance less than 3mm. A sourcemeter was connected in series to the pearl chain to supply current to the circuit and measure the voltage change. Constant current of 40μA was applied to the circuit.

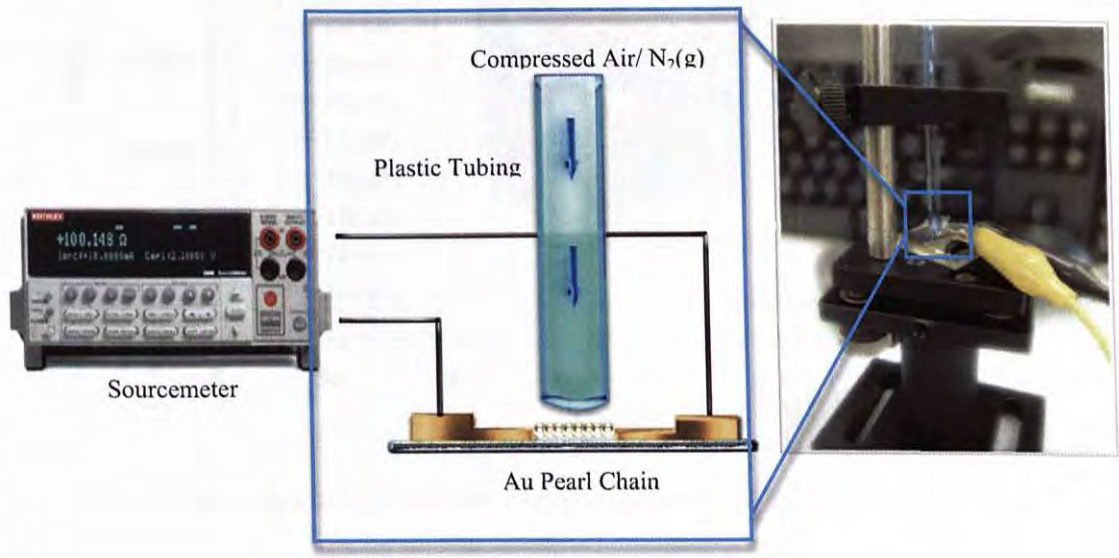

Figure 30 Experimental setup for testing airflow sensing

7.2 Experimental Results

7.2.1 Sensor Response to Air

The experiment results in Figure 31 show that the measured resistance change ($\Delta R/R_o$, R_o is assumed as the resistance measured at the instant that airflow is introduced onto the sensor) dropped when airflow was injected onto the sensor and it rose again when the airflow was stopped. The resistance change increased with the input air pressure. The measured resistance change in between the start and stop of airflow injection was averaged and plotted in Figure 32 against the gas pressure. On average the resistance change varies from -0.001 to -0.0035 (-0.1% to -0.35%) when the input pressure varies from 100kPa to 170kPa. The resistance change drops linearly with the input pressure. When the air pressure increases, the resistance changes drops more rapidly.

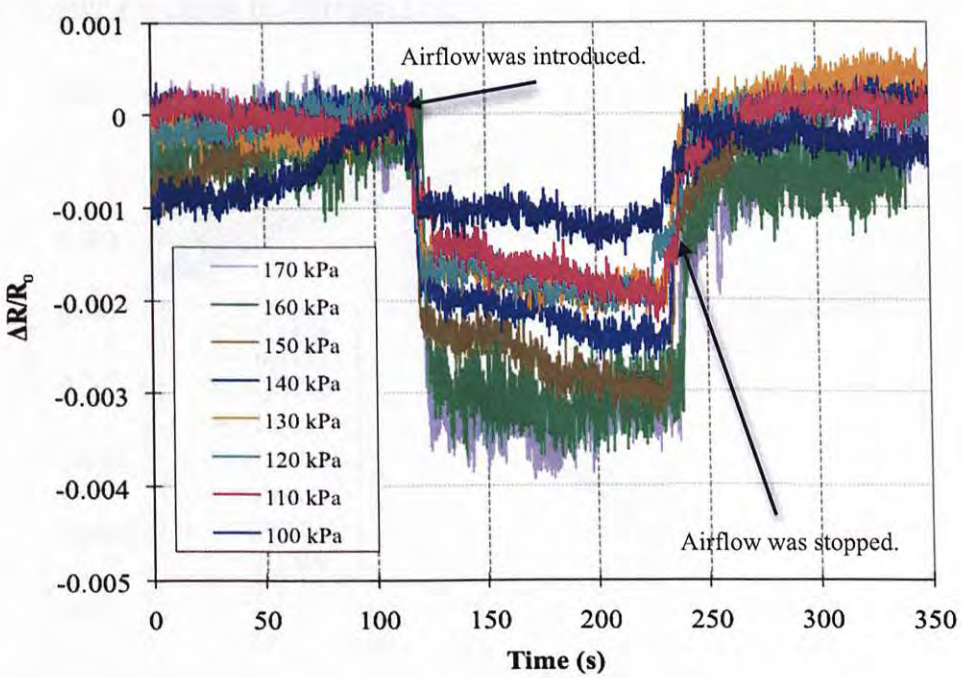

Figure 31 Resistance change of the AuNP based sensor under airflow at varying pressure

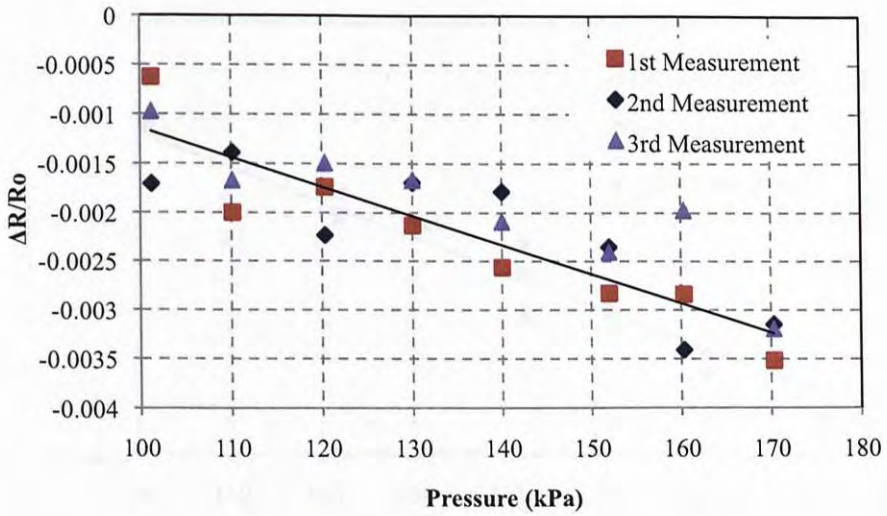

Figure 32 Resistance change-air pressure dependency of the sensor

7.2.2 Sensor Response to Nitrogen Gas

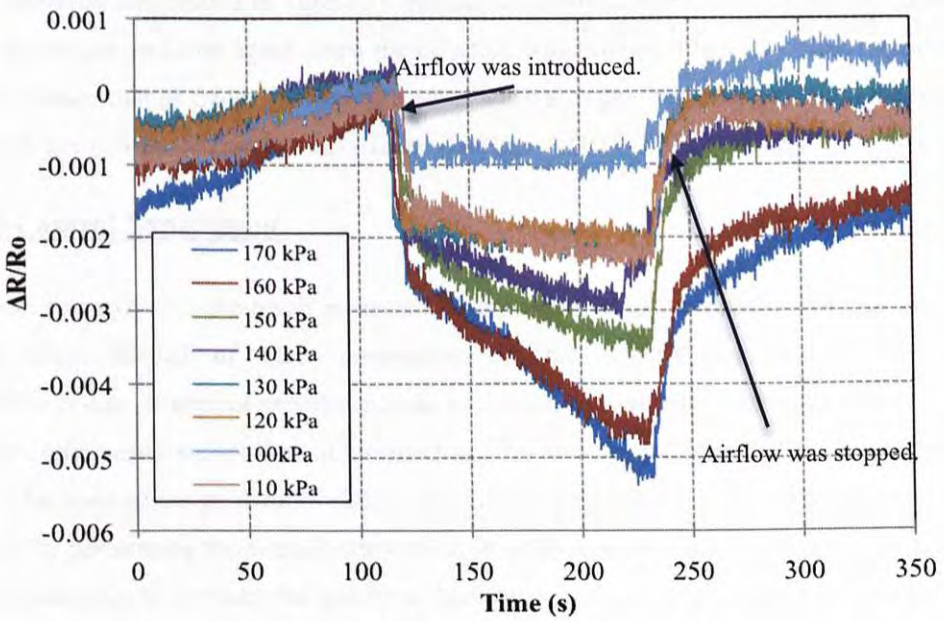

Figure 33 Resistance change of the AuNP based sensor under N_2(g) at varying pressure

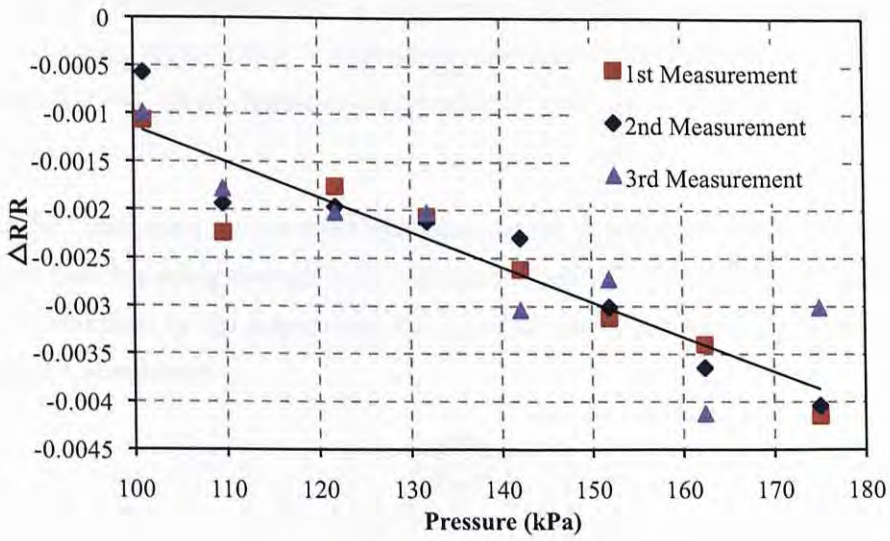

Figure 34 Resistance change-nitrogen gas pressure dependence of the sensor

Another experiment was performed by injecting nitrogen gas onto the sensor. Similar results were achieved and plotted in Figure 33. Resistance dropped when nitrogen gas was injected onto the sensor and rose again when the injection was stopped. Figure 34 plots the average the resistance change under different pressures when nitrogen gas is injected onto the sensor. The average resistance change varies from -0.001 to -0.004 (-0.1% to -0.4%).

7.2.3 Control Experiment

In order to verify that the result measured by the sensor chips was responsible for the gold pearl chain instead of other components of the sensors, for example the gold microelectrodes. A control experiment was performed to study the electrical response of the sensor components except the gold pearl chain. Without the gold pearl chain linking up the microelectrode gap, a gold microwire (as shown in Figure 35) was fabricated to complete the circuit for performing the control experiment. In order to draw a more conclusive result, it is more preferable to conduct the test by a fabricated gold nanowire instead of a microwire. However, fabrication of gold nanowire through electron beam lithography is technically challenging.

The resistance change of the control device was measured by the sourcemeter. According to Figure 37, the slope of resistance change against pressure is similar for both the control device (microwire) and the Au-NP based sensor under the same kind of gas flow. However, the control is less responsive. It is possibly because of the gold pearl chain is responsible to other physical phenomena besides temperature when subject to gas flow. Further research is required for understanding the reason why pearl chain structure increase sensor

responsibility. By comparing Figure 31 with Figure 36, the gold pearl chain gives a sharper resistance change when airflow is injected onto the sensor. The difference is more obvious by comparing the sensor response against airflow with low injected pressure (e.g. 100-110kPa).

The Au-NP based senor gives a more significant change in resistance than the control device when gas flow is passing through it. In conclusion, it proves that the response of the sensor chips is dominated by the response of the gold pearl chain instead of the response of the other sensor components.

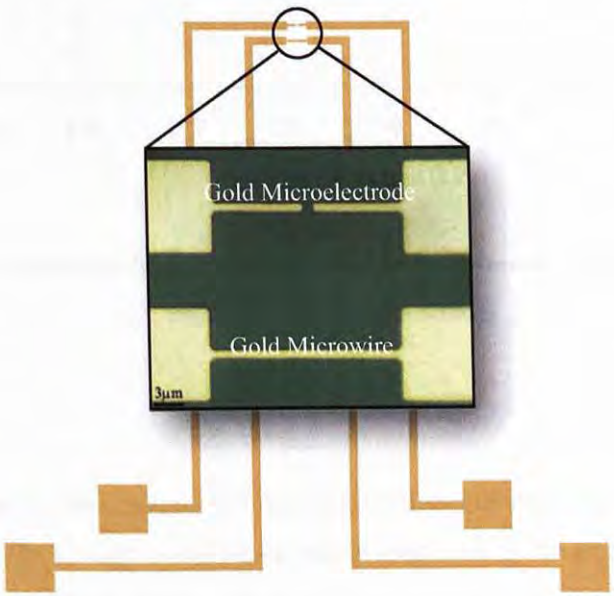

Figure 35 Comparison of gold microelectrode and gold microwire

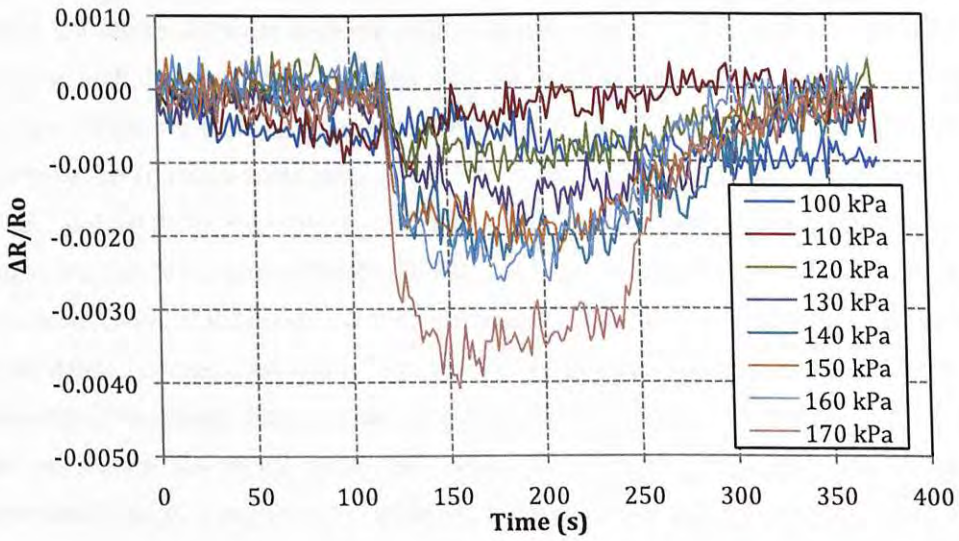

Figure 36 Resistance change of the gold microwire under airflow at varying pressure

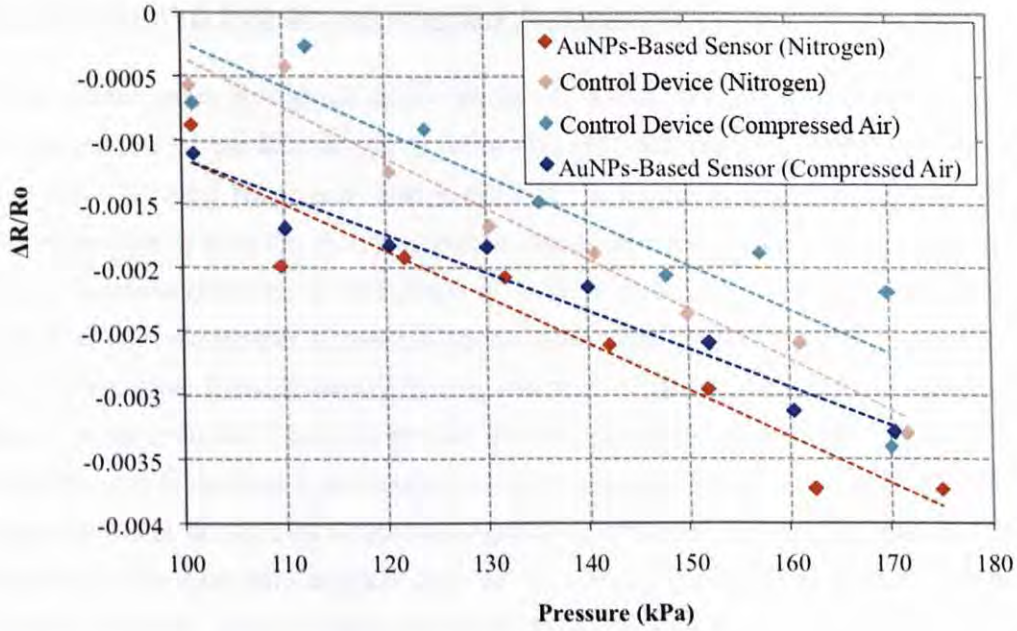

Figure 37 Electrical response of the AuNP based sensor and the microwire under air or nitrogen gas flow

7.3 Discussions

Figure 32 and Figure 33 demonstrate that our sensor is feasible to distinguish gas flow under different pressure. The change in resistance was proportional to the amplitude of the input pressure. Large background noise, signal drift and declination were observed in the experimental results. These phenomena are possibly contributed by the measuring equipment, environment and inherent disturbance. To verify the source of disturbance, we compare the sensor response with the control device response. The level of disturbance is similar for both devices, which conclude that the inherent noise of the gold pearl chain is rather low. When we took 1000 resistance samples for around 1700s under room condition to compute the signal-to-noise ratio. The SNR of the gold pearl chain and microwire was 76.47dB and 70.05dB respectively. Compare with sensors form by other materials, for example, the EG-CNTs sensor (SNR = 56.2dB), our sensor is relatively stable [35]. Since the environment is one of the major possibility to induce the disturbances, a more linear pressure and resistance change relationship is potentially to be observed by better controlling the experimental conditions. For example integrating the sensor into a PMMA microchannel in order to reduce the noise from the environment. Further research with advanced experimental design is required for achieving a complete study of this sensor. In this work, we successfully proof that our device is feasibly to work as an airflow sensor.

7.3.1 Relationship between the Measured Electric Response and Temperature

When airflow passes through the sensor, the environmental temperature is lowered because the temperature of the injected gas is lower than the environmental temperature. In our experiment, the room temperature was around 23°C. When gases at different pressures were injected into the system, the room temperature change around the sensor was measured by a K-type thermocouple with an error range of -0.05 °C to 0.04 °C. The thermocouple was connected to a sourcemeter in constant current mode. The voltage-temperature relationship of a thermocouple is non-linear and has the character of a polynomial [36]. The details are shown in Appendix-III. When compressed air and nitrogen gas at different pressures were injected on top of the sensor, the change in room temperature was measured and is plotted in Figure 38. When the injected air pressure varied from 100kPa to 170kPa, the environmental temperature approximately dropped from 0°C to 1.8°C, whereas the temperature dropped from 0°C to 2.3°C when nitrogen gas with 100kPa-170kPa pressure was injected into the system.

Assuming that all the electrical responses measured from the AuNP based sensor were induced by the change of environmental temperature around the sensor, according to the TCR of the gold pearl chain and microwire as shown in Figure 29, the temperature change can be estimated by the measured resistance change using equation (14). The estimated temperature of the Au pearl chain and microwire are plotted in Figure 38. For microwire, the temperature dropped from 0.2°C to 2.2°C and from 0.3°C to 2.6°C when compressed air and nitrogen gas at various pressures were injected onto it respectively. For the Au pearl chain, the estimated environmental temperature dropped from 1.15°C to 3.15°C and from 1.15°C to 3.75°C when experiencing compressed air and nitrogen gas respectively.

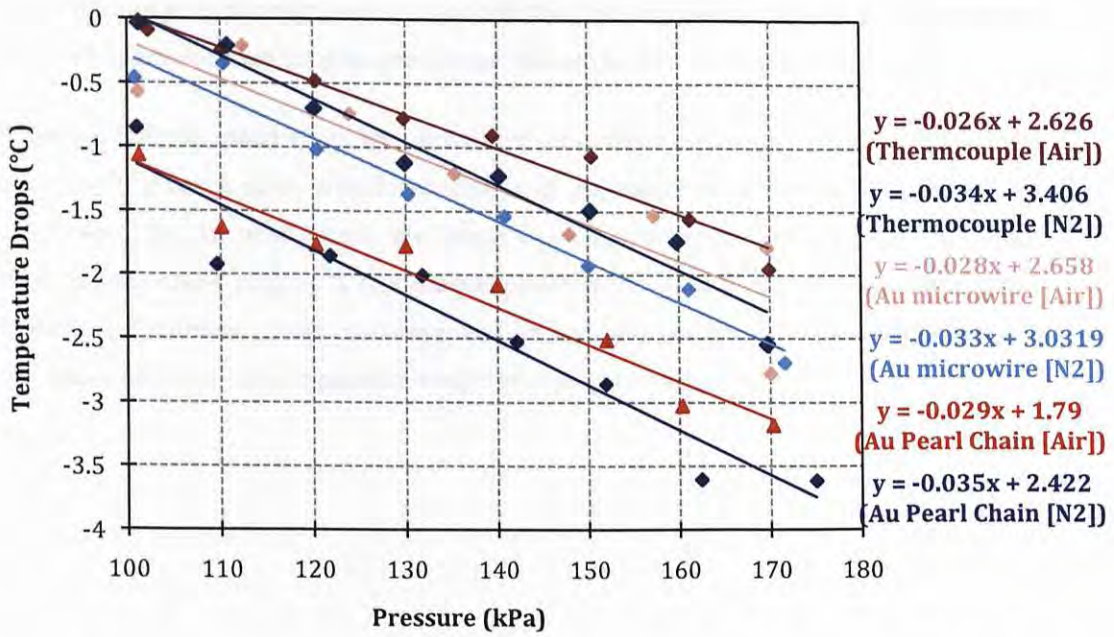

Figure 38 Temperature change against gas pressure (compressed air and nitrogen gas) measured by different kinds of sensing element, including thermocouple, Au microwire and Au pearl chain.

7.3.2 Pressure-Temperature Relationship of the Sensor

The experimental results measured by the thermocouple imply that the environmental temperature decreases with the input gas pressure. Temperature drops because of the heat loss induced by the airflow. Under the same gas pressure, nitrogen gas lowers the environmental temperature more than compressed air since the temperature of nitrogen gas is lower than air under the same pressure and volume. As stated by the Ideal Gas Law,

$$P = \frac{\rho}{M} RT \qquad (15)$$

where P is the absolute pressure of the gas, m is the mass of the gas, M is the molar mass of the gas, R is the universal gas constant and T is the absolute temperature. Under the same volume and pressure, the ratio of density to molar mass for nitrogen and air is equal to 0.04465 and 0.04463 respectively, indicating that the temperature of nitrogen is lower than air under the same conditions.

Comparing the slope of the trend lines in Figure 38, a similar slope is obtained for the same kind of gas sensed by different materials (thermocouple, Au microwire and Au pearl chain) minus the measured temperature drop at different pressures by the initial temperature drop measured in 100kPa. All the sensing elements measure a similar dropping range, approximately 0°C to 2°C for air and 0°C to 2.3°C for nitrogen. Using the results from the

thermocouple as a reference, we can conclude that both microwire and pearl chain can detect the level of environment temperature change induced by airflow at different pressures.

Although both the pearl chain and microwire sense the pressure difference of airflow, the pearl chain gives a more significant change in resistance as shown in section 7.2.3. In conclusion, the Au pearl chains are found to be novel sensing elements for low power thermal and airflow sensors. A fundamental prototype for an airflow sensor was successfully fabricated. Preliminary tests on compressed air and nitrogen gas flow were performed and the sensor obtained a linear pressure-temperature relationship.

8. Conclusion

Fabrication of gold nano-particle based sensors by combining microspotting and DEP technologies is presented in this dissertation. With a microspotting system, gold pearl chains can be rapidly and precisely formed across microelectrodes with a low production cost. DEP technology forms gold nanoparticle chains consistently between microelectrodes in a single step. To investigate the optimal condition for particle chain formation (PCF), a systematic experimental study together with a theoretical analysis of the dominant force, which manipulate the AuNPs' movement in the DEP frequency range from 1Hz to 10MHz was performed. At low frequency level, pearl chain formation could not be observed because of the fluid motion and negative DEP force. Fluid motion induced by both AC electroosmosis and electrothermal body force opposes DEP manipulation. Moreover, the applied potential drops across the double layer and the magnitude of the DEP force is lowered. When the frequency of applied electric field increases, the AC electroosmotic effect decreases significantly and the fluid flow induced by electrothermal force changes its direction to enhance DEP manipulation. Eventually, PCF is observed in a specific frequency range in between the low and high frequency region. At high frequency levels, particles experience negative DEP force again and are repelled from the microelectrodes; therefore no PCF was observed in our experiments. The optimum frequency for manipulating 10nm and 100nm AuNPs are 50kHz and 100kHz, respectively, and the optimum voltage is in the range of $12V_{pk\text{-}pk}$ to $16V_{pk\text{-}pk}$. The I-V characteristics and TCR of the AuNP based sensors indicate that the gold pearl chain has the potential to serve as a lower power thermal sensor. Experiments on sensor response against airflow at various pressures were also performed. A promising result shows that the air pressure is directly proportional to the sensor response. A linear pressure-resistance relationship was observed from the sensor based on its excellent thermal responsivity. In conclusion, gold nano-particle based thermal sensors can be successfully fabricated by combining DEP and microspotting technologies.

9. Future Work

9.1 DEP Manipulation of 2nm diameter gold nanoparticles

Nowadays, only a few researchers report that AuNPs with diameters smaller than 10nm can be manipulated across microelectrodes by DEP force. Gold nanoparticles with smaller diameters are more difficult to manipulate since the magnitude of other forces is higher than or similar to the DEP force. However, manipulation of 2nm AuNPs is known as an important technology for miniaturizing nano-devices in the future. Ideally, the fabrication cost, amount of sample and response time can be reduce by device miniaturization.

In order to investigate the possibility of 2nm AuNP based pearl chain formation, a theoretical simulation was performed followed by experimental verification. In the theoretical simulation, we assumed that the condition of the 2nm gold solution is the same as the 10nm and 100nm solution except that the particle size is smaller and the medium conductivity is lower as the concentration of gold chloride in 2nm solution is lower than the 10nm and 100nm solution. If the input potential is $16V_{pk\text{-}pk}$, the maximum fluid flow rate induced by AC electroosmosis and electrothermal force is in the order of 10^{-6} and 10^{-4} respectively when the input frequency is higher than 1kHz. The magnitude of the particle velocity induced by DEP force is in the order of 10^{-5} as shown in Figure 39. In certain frequency ranges, particle velocity induced by particle velocity induced by DEP force is higher than the fluid flow velocity, and thus, pearl chains can theoretically be formed. A preliminary experiment of gold pearl chain formation by 2nm AuNPs was performed. Pearl chains were successfully formed between microelectrodes under $16V_{pk\text{-}pk}$ input voltage and 150kHz input frequency. The SEM image is shown in Figure 40. Surprisingly, the pearl chain formed by 2nm AuNPs is apparently difference from those formed by 10nm or 100nm AuNPs. Highly branched structure is obtained and pearl chain seems to grow from one direction to another. To understand more on 2nm AuNP based PCF, more systematic experimental study and theatrical analysis will need to be performed.

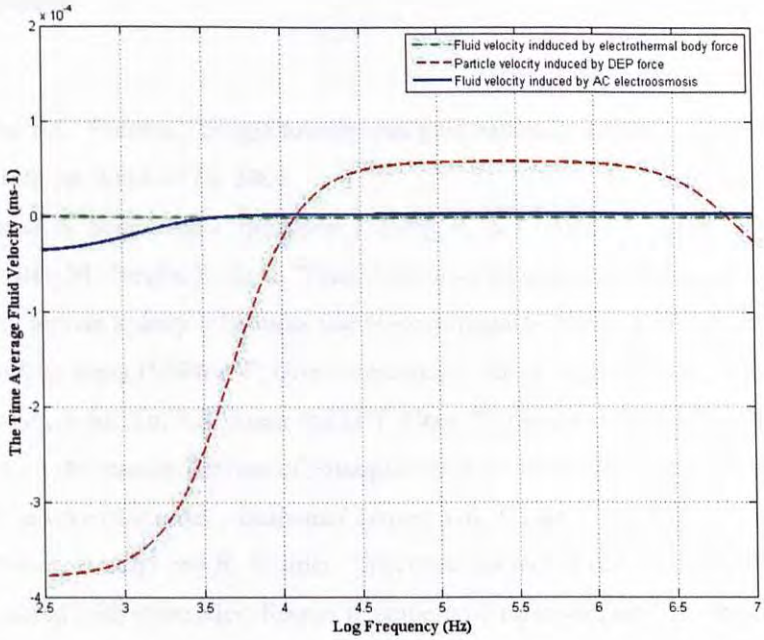

Figure 39 Comparison of particle velocity against fluid flow velocity at the middle of the electrode gap for 2nm AuNPs suspended in D.I. water

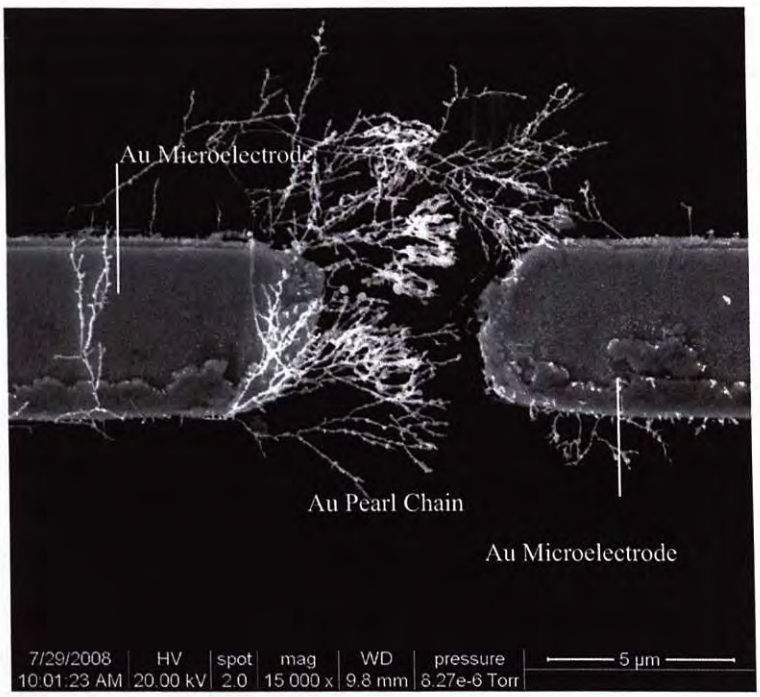

Figure 40 SEM image of gold pearl chains formed by 2nm AuNPs

References

[1] Z. Liu, P.C. Searson, "Single nanoporous gold nanowire sensors", *J. Phys. Chem. B* , vol. 110, pp. 4318-4322. 2006

[2] M. Basu, S. Seggerson J. Henshaw, J. Jiang, R. A. Cordona, C. Lefave, P. J. Boyle, A. Miller, M. Purgia, S. Basu, "Nano-biosensor development for bacterial detection during human kidney inflection: use glycoconjugate-specific antibody-bound gold NanoWire array (GNWA)", *Glycoconjugate J.* vol. 21, pp. 487-496, 2004

[3] Y.H. Gu, A.M. Yu, S.S. Yuan and H.Y. Chen, "Amperometric nitric oxide biosensor based on the immobilization of hemoglobin on a nanometer-sized gold colloid modified Au electrode", *Analytical Letters,* vol. 35, iss. 4, pp. 647-661, 2002

[4] I. Willner, E. Katz and B. Willner, "Electrical contact of redox enzyme layers associated with electrodes: Routes to amperometric biosensors" *Electroanalysis,* vol.9, pp. 965-977, 1997

[5] J.K.N. Mbindyo, B.D. Reiss, B.R. Martin, C.D. Keating, M.J. Natan, T.E. Mallouk, "DNA-directed assembly of gold nanowires on complementary surfaces", *Adv. Mater.,* vol.13, pp. 249–254, 2001

[6] S. Keebaugh, A.K. Kalkan, W.J. Nam, S.J. Fonash, "Gold nanowires for the detection of elemental and ionic mercury", *Electrochem. Solid-State Lett.*, vol. 9, H88–H91, 2006

[7] N.I. Kovtyukhova, T.E. Mallouk, "Nanowires as building blocks for selfassembling logic and memory circuits", *Chem. Eur. J.*, vol.8, pp.4355–4363, 2002

[8] C.D. Keating, M.J. Natan, "Striped metal nanowires as building blocks and optical tags", *Adv. Mater.*, vol. 15, pp. 451–454, 2003

[9] S. Aravamudlhan, N. S. Ramgir, S. Bhansali, "Electrochemical biosensor for targeted detection in blood using aligned Au nanowires", *Sensors and Actuators B,* pp. 29-35, 2007

[10] Y. J. Kim, S. M. Cho, H. B. Pyo, C. A. Choi, "Sub-ppm detection of gold nanoparticle transducer toward carboxyl functionality" , *IEEE Sensors,* 2005

[11] N. Nath, A. Chilkoti, "A colorimetric gold nanoparticle sensor to interrogate biomolecular interactions in real time on a surface", *Analytical chemistry*, vol. 74, no. 3, pp. 504-509, 2002

[12] R. G. Grainger, "Intravascular Contrast Media—the Past, the Present, and the Future," *Br. J. Radiol.*, vol. 55, no. 1, 1982.

[13] L. F. Zheng, S. D. Li and P. J. Burke, "Self-Assembled Gold Nanowire from Nanoparticles: An Electronic Route Towards DNA Nanosensors," *Nanoengineering: Fabrication, Properties, Optics and Devices,* SPIE vol. 5515, 2004.

[14] G. W. Leung, F. T. Lau, S. L. Leung and W. J. Li, "Formation of Au Colloidal Crystals for Optical Sensing by DEP-Based Nano-Assembly," *The 2nd IEEE Conference on Nano/Micro Engineered and Molecular Systems,* January 16, 2007.

[15] S. I. Khondaker, "Fabrication of Nanoscale Device Using Individual Colloidal Gold Nanoparticles," *IEE Proc-Circuits Devices Syst.*, vol. 151, no.5, 2004.

[16] R. S. Wagner and W. C. Ellis, "Vapor-Liquid-Solid Mechanism of Single Crystal Growth," *Applied Physics Letters,* Vol.4, No.5, 1964.

[17] M. Calleja, M. Tello, J. Anguita, F. Garcı´a and R. Garcı´a, "Fabrication of gold nanowires on insulating substrates by field-induced mass transport", *Applied Physics Letter,* vol. 79, no. 15, pp. 2471–2473, 2001

[18] Q. Xu, L.Bao, F. Capasso and G. M. Whitesides, "Surface Plasmon Resonances of Free-Standing gold Nanowires Fabricated by Nanoskiving", *Angew. Chem,* vol. 118, pp. 3713-3717, 2006

[19] M. Watanabe, H. Minoda and K.Takayanagi, "Fabrication of Gold Nanowires Using Contact Mode Atomic Force Microscope", *Jpn. J. Appl. Phys.,* Vol. 43, pp. 6347-6349, 2004

[20] Q.Xu, R. Perez- Castillejos, Z. Li and G. M. Whitesides, "Fabrication of High-Aspect-Ratio Metallic Nanostructures Using Nanoskiving", *Nano Lett.,* vol. 6, iss. 9, pp. 2163 -2165, 2006

[21] R. Kretschmer and W. Fritzsche, "Pearl chain formation of nanoparticles in microelectrode gaps by dielectrophoresis," *Langmuir*, vol. 20, no. 26, pp. 11797-801, 2004

[22] H. A. Pohl, "Dielectrophoresis," *Cambridge: Cambridge University Press,* 1978.

[23] A. Ramos, H. Morgan, N. G. Green and A. Castellanos, "AC Electrokinetics: a review of forces in microelectrode structures", *J. Phys. D: Appl. Phys*, vol. 31, 1998.

[24] J. D. Gibson, B. P. Khanal and E. R. Zubarev, "Paclitaxel-Functionalized Gold Nanoparticle" J. Am. Chem. Soc., vol. 129, pp. 11653-11661, 2007

[25] "Gold is newest weapon in battle against Alzheimer's", *Health News, FindArticles.com.,* 26 Oct. 2006
http://findarticles.com/p/articles/mi_m0857/is_3_12/ai_n17212704

[26] X. Qian, "In vivo tumor targeting and spectroscopic detection with surface-enhanced Raman nanoparticle tags." *Nature Biotechnology*, vol. 26 no. 1, 2008

[27] B. Wessling, "Conductive Polymer / Solvent Systems: Solutions or Dispersions?", 1996
http://www2.ormecon.de/Research/soludisp/

[28] "Colloidal gold", *Wikipedia*
http://en.wikipedia.org/wiki/Colloidal_gold

[29] M. P. Hughes, "AC Electrokinetics: Applications for Nanotechnology," *Nanotechnology*, vol. 11, pp. 124–132, 2000.

[30] M. L. Li, F. Fei, Y. L. Qu, Z. L. Dong, W. J. Li and Y. C. Wang, "Theoretical Analysis Based on Particle Electro-Mechanics for Au Pearl Chain Formation," *The 7th IEEE International Conference on Nanotechnology*, August 03, 2007.

[31] J. Clendenin, H. Rokadia, S. Tung and K. Ogburia, "Application of aligned carbon nanotubes in micro shear stress sensing", *The International Mechanical Engineering Congress and RD&D Expo*, IMECE2004-61227, November 13-19, 2004

[32] H. Morgan and N. G. Green, "AC Electrokinetics colloidal and nanoparticles", *Research Studies Press Ltd.*, 2003

[33] W. C. Lai, K. M. Fung and W. J. Li, "A Systematic Approach to Fabricate CNT-Based Nano Devices: Combining DEP and Microspotting Techologies," *The 5th IEEE International Conference on Nanotechnology,* July 11, 2005

[34] http://www.science.uwaterloo.ca/~cchieh/cact/c123/nernsteq.html

[35] M. Ouyang, M. L. Y. Sin, G. C. T. Chow, W. J. Li, X. Han, D. C. Janzen, "DEP-Based Fabrication and Characterization of Electroic-Grade CNTs for Nano-Sensing Applications," *The 7th International Conference on Nanotechnology*, August 3, 2007

[36] "Thermocouple", *Wikipedia*
http://en.wikipedia.org/wiki/Thermocouple

[37] T.B. Jones, "Electromechanics of particles", *Cambridge, New York, Cambridge University Press*, 1995

[38] "Gibbs free energy", *Wikipedia*
http://en.wikipedia.org/wiki/Gibbs_free_energy

[39] http://www.chem1.com/acad/webtext/elchem/ec4.html

[40] http://srdata.nist.gov/its90/main/

List of Publications

Conference paper

Siu Ling Leung, Minglin Li, Fong Ting Lau and Wen J. Li, "Fabrication of Gold Nano-Particle Based Sensors Using Microspotting and DEP Technologies," SICE Annual Conference 2008: International Conference on Instrumentation, Control and Information Technology, August 22, 2008.

Siu Ling Leung, Ming Lin Li and Wen J. Li, "Formation of Gold Nano-particle Chains by DEP – a Parametric Experimental Analysis," The 3rd IEEE International Conference on Nano/Micro Engineered and Molecular Systems, January 09, 2008.

Gong Wai Leung, Fong Ting Lau, Siu Ling Leung and Wen J. Li, "Formation of Au Colloidal Crystals for Optical Sensing by DEP-Based Nano-Assembly," The 2nd IEEE Conference on Nano/Micro Engineered and Molecular Systems, January 16, 2007.

APPENDIX-I The Clausius-Mossoti (CM) Factor

I-1 The CM factor of homogeneous dielectric spheres

Dr. T.B. Jones published the simulation of the CM factor of homogeneous dielectric spheres in Cambridge University Press 1995.

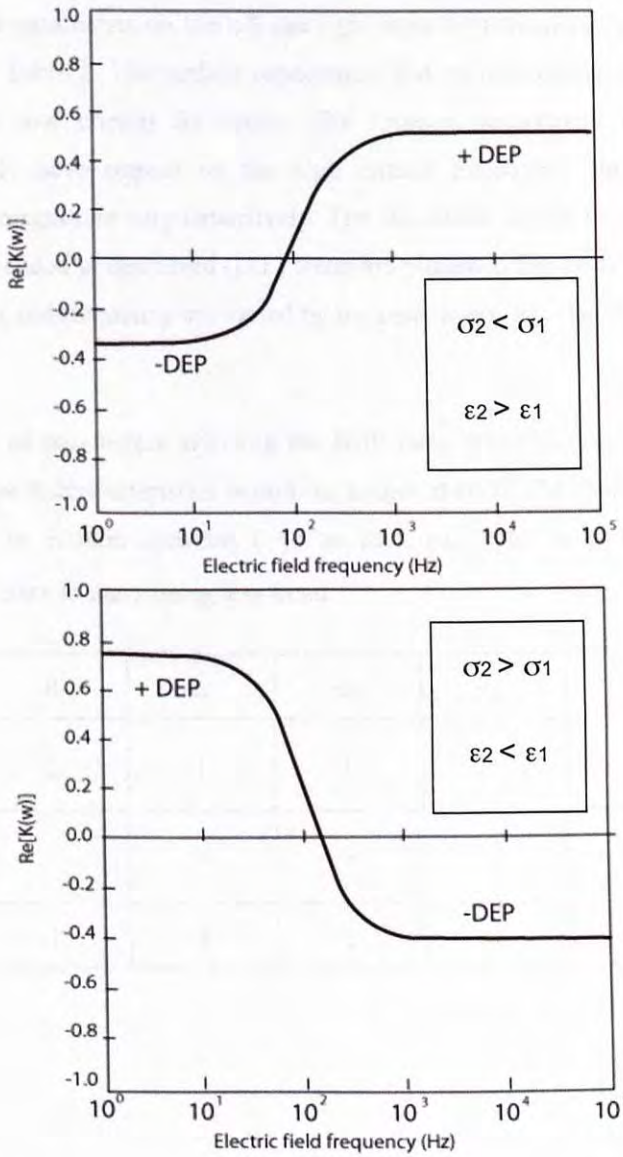

Figure 41 Dielectrophoretic spectra of homogeneous dielectric spheres with ohmic loss, where ε_1, ε_2 is the permittivity of the core sphere and thin surface layer respectively. σ_1, σ_2 are the conductivity of the of the core sphere and thin surface layer respectively [37]

I-2 The CM factor of a single shell sphere

For a single shell model, the CM factor is influenced by the particle radius (R), surface conductivity of the thin surface layer (c_s), external medium conductivity (σ_m), external medium permittivity (ε_m), core sphere conductivity (σ_c) and core sphere permittivity (ε_c). Our collaborator Mr. Minglin Li in State Key Laboratory of Robotics in SIA, CAS, performed the simulation on the effect of each parameter.

The effects of these parameters on the left and right cross over frequency and the magnitude are summarized in Table 2. The surface capacitance and solution conductivity are of major importance to the low critical frequency. The solution permittivity and core particle conductivity mainly have impact on the high critical frequency. The effects of these parameters on the magnitude vary extensively. The simulation results for gold colloids with size of 100nm suspended in deionized (D.I.) water are plotted in Figure 42. It shows that not only the magnitude and frequency are varied by the parameters, but also the peak of maxima is affected.

Table 2 Summary of parameters affecting the DEP force spectrum: the general trends are given for three growth characteristics within the ranges studied. The characteristics increase (↑), decrease (↓) or remain constant (−) as each parameter is increased. Additional characteristic (ñ) refers to there being less trend.

Parameters	R	c_s	σ_m	ε_m	σ_c	ε_c
f_{low} ↑	↓	↓	↑	−	−	−
f_{high} ↑	−	−	−	↓	↑	ñ
Magnitude ↑	↑	↑	↓	↓	↑	−

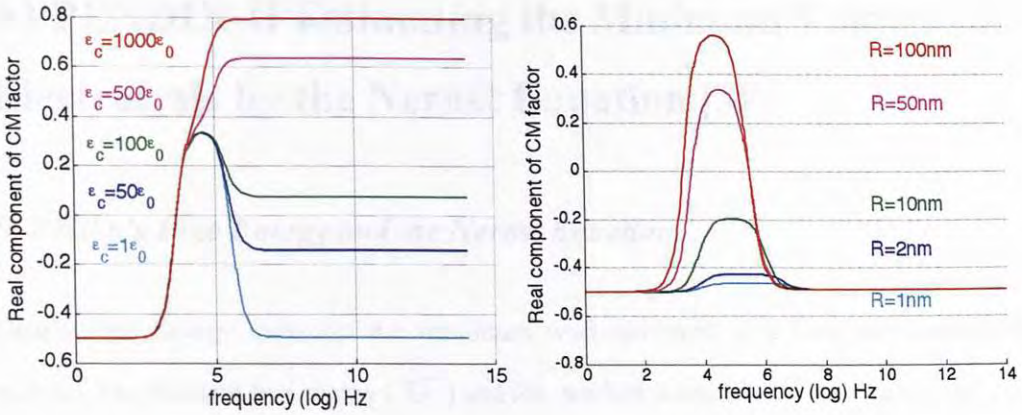

(a) (b)

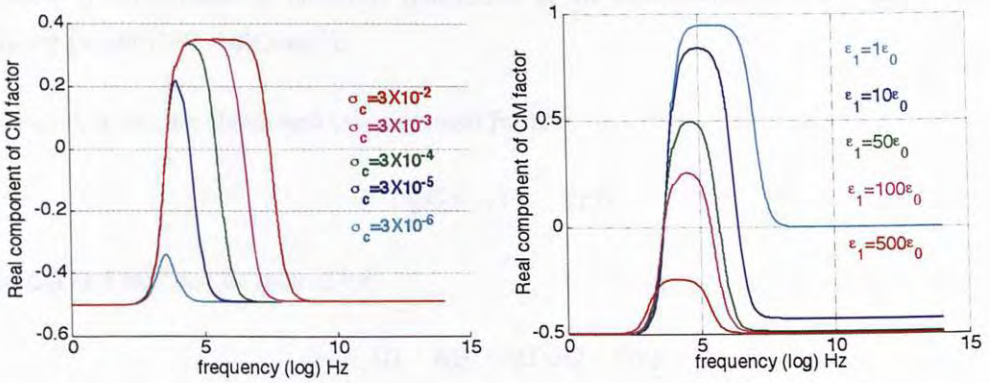

(c) (d)

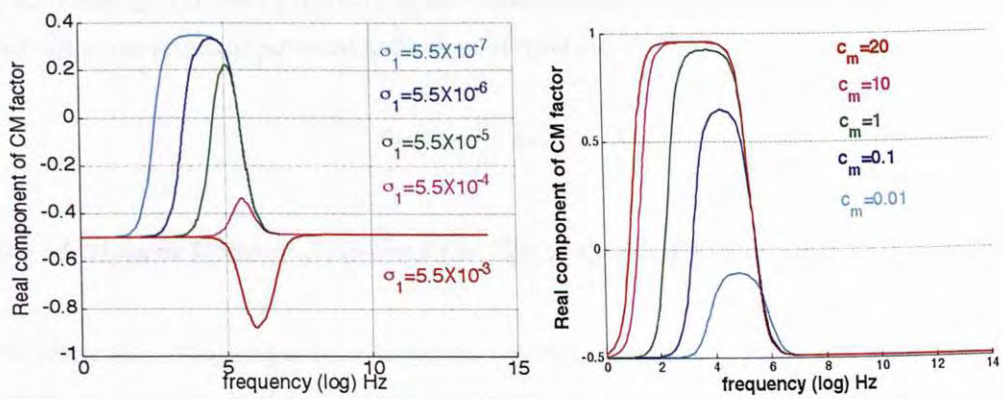

(e) (f)

Figure 42 The real CM factor versus frequency by varying the (a) core sphere permittivity, (b) particle radius, (c) surface conductivity of the thin surface layer, (d) medium permittivity, (e) medium conductivity and (f) core sphere conductivity [30]

APPENDIX-II Estimating the Minimum Voltage for Electrolysis by the Nernst Equation [39]

II-1 Gibb's Free Energy and the Nernst Equation

Gibb's Free Energy measures the maximum work achieved in a completely reversible process. The standard free energy (G°) and the standard potential (E°) are related by:

$$\Delta G^\circ = -nFE^\circ \quad (16)$$

where n is the number of electrons transferred in the half-reaction and F is the Faraday constant ($9.6485307\times10^4 Cmol^{-1}$).

The equation can be elaborated into a general form:

$$\Delta G = -nFE \quad (17)$$

and ΔG and ΔG° can be related by:

$$\Delta G = \Delta G^\circ + RTInQ \quad (18)$$

where, R is the gas constant, T is the temperature and Q is the reaction quotient [38].

By substituting (17) into (15) and (16), the Nernst equation is obtained, which relates the cell potential to the standard potential and extent of reaction.

$$E = E^\circ - \frac{RT}{nF} InQ \qquad (19)$$

II-2 Minimum Voltage Required for Electrolysis of Water with Different pH

The minimum voltage input for electrolysis can be determined by the Nernst equation. The amount of electrical energy required for electrolysis is equal to the change in Gibb's free energy plus the losses (theoretically close to zero) in the system. However, the theoretically predicted value would be lower than the actual value, which depends on the electrode distance and ion concentration.

During electrolysis of water, hydrogen and oxygen gas are released as stated in the following two half equations:

Reduction reaction: $2H^+ + 2e^- \rightarrow H_2(g)$

Oxidation reaction: $2H_2O \rightarrow O_2(g) + 4H^+ + 4e^-$

Applying the Nernst equation to both the reduction and oxidation reaction at 25°C,

$$E_{H^+/H_2} = E^o_{H^+/H_2} - \frac{RT}{nF} In\left(\frac{[H^+]^2}{P_{H_2}}\right)$$

$$E_{O_2/H_2O} = E^o_{O_2/H_2O} - \frac{RT}{nF} In\left(P_{O_2}[H^+]^4\right)$$

then,

$$E_{H^+/H_2} = E^o_{H^+/H_2} - (0.0295) \times 2pH = -0.059pH$$

$$E_{O_2/H_2O} = E^o_{O_2/H_2O} - 0.0295 \times 2pH = 1.23 - 0.059pH$$

Balancing the oxidation and reduction equation, the minimum voltage for electrolysis of water is 1.23V. The pH value of the solution does not vary the minimum voltage since the pH factor is cancelled out. The stability diagram of water is shown in Figure 43.

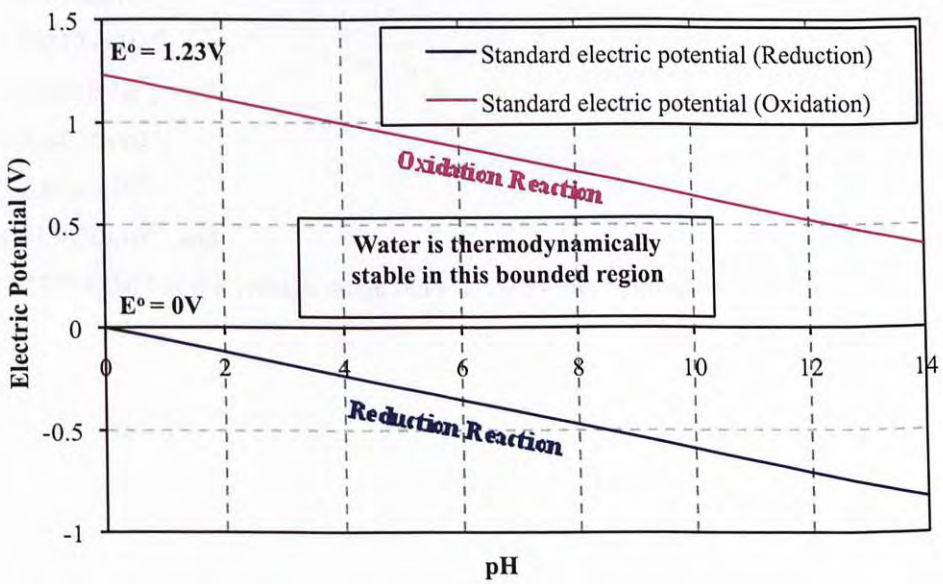

Figure 43 Stability diagram of water

Appendix-III Temperature-Voltage Relationship of the K-type Thermocouple [40]

Generally, the relationship between the temperature difference and the output voltage of a thermocouple is non-linear and is approximated by the polynomial:

$$\Delta T = \sum_{n=0}^{N} d_n V^n \quad (20)$$

where d_n is the coefficient given for N from zero to between five and nine [36].

For K-type thermocouples, the voltage-temperature relationship above 0°C is given by:

$$\Delta T = d_0 + d_1 V + d_2 V^2 + ...d_n V^n \qquad (21)$$

where:

$d_0 = 0$;
$d_1 = 2.508355 \times 10^{1}$;
$d_2 = 7.860106 \times 10^{-2}$;
$d_3 = -2.503131 \times 10^{-1}$;
$d_4 = 8.315270 \times 10^{-2}$;
$d_5 = -1.228034 \times 10^{-2}$;
$d_6 = 9.804036 \times 10^{-4}$;
$d_7 = -4.413030 \times 10^{-5}$; and
$d_8 = 1.057734 \times 10^{-6}$ in the voltage range 0mV to 20.644mV with an error range of -0.05°C to 0.04°C.

Appendix-IV Mathlab Program

IV-1. Fluid velocity induced by AC electroosmosis

```
ome = [3.5:1:1000,1e3:100:1e5,1e5:1e5:1e10];
%ome = [1e3:100:1e7];
% Gobal variables
eps_m = 80*8.85e-12; % the relative dielectric constant of the medium.
sig_m = 5e-5; % the conductivity of the medium
Pi=3.14;
Vis = 8.9e-4; % Viscosity of the medium
Vrms = 14; % RMS of input voltage
Ang_f = 2*Pi*ome; % Angular Frequency
ion_L= 6e-4; % ionic strength
x_L = 0.7e-6; % distance from electrode
De_L =1/(3.288*sqrt(ion_L)*1e-9); % debye length
% Calculate fluid velocity generated by AC electroosmosis
Ohm = 0.5*Pi*De_L*x_L*Ang_f*(eps_m/sig_m);
V_Eosm=(eps_m*(Vrms^2/2)*Ohm.^2)./(8*Vis*x_L*(1+Ohm.^2).^2);
figure (1)
hold on, grid on, box on
plot (log10(ome), V_Eosm,'g', 'Line Width', 1.5)%, 'Marker', 'o'
xlabel ('Log Frequency')
ylabel ('The Time Average Fluid Velocity (ms-1)')
legend ('Fluid velocity induced by AC electroosmosis')
```

IV-2. Voltage drop across the double layer

```
ome = [0:1:1000,1e3:100:1e5,1e5:1e5:1e7];
% Gobal variables
eps_m = 80*8.85e-12; % the relative dielectric constant of the medium.
sig_m = 5.5e-6; % the conductivity of the medium
Pi = 3.14;
Vis = 8.9e-4; % Viscosity of the medium
Vrms = 12; % RMS of input voltage
Ang_f = 2*Pi*ome; % Angular Frequency
```

```
ion_L = 6e-4; % ionic strength
x_L = 1e-6; % distance from electrode
De_L =1/(3.288*sqrt(ion_L)*1e-9); % debye length
Rv = Vrms/sqrt(2)
% Calculate fluid velocity generated by AC electroosmosis
Double_V = ((Vrms/sqrt(2))./(2+(sqrt(-1)*Ang_f*Pi*(eps_m/sig_m )*De_L*x_L)));

figure (2)
hold on, grid on, box on
plot (log10(ome), real(Double_V), 'Line Width',1.5)%, 'Marker', 'o'
xlabel ('Log Frequency')
ylabel ('Potential Drop Across Double Layer (V)')
```

IV-3. Fluid velocity induced by electrothermal force

```
ome = [1:10:1000,1e3:100:1e5,1e5:1e5:1e10];
%ome = [1e3:100:1e7];
% Gobal variables
eps_m = 80*8.85e-12; % the relative dielectric constant of the medium.
sig_m = 5e-5; % the conductivity of the medium
Pi = 3.14;
Vis = 8.9e-4; % Viscosity of the medium
Vrms = 14/sqrt(2); % RMS of input voltage
Ang_f = 2*Pi*ome; % Angular Frequency
ion_L= 6e-4; % ionic strength
x_L = 1e-6; % distance from electrode
De_L = 1/(3.288*sqrt(ion_L)*1e-9); % debye length
Arf = -0.004;
Beta = 0.02;
Thc_m = 0.6;
R = 50e-6;
C = (Ang_f*(eps_m/sig_m)).^2;
% Calculate fluid velocity generated by Electrothermal Force
M_Factor = ((Arf-Beta)./(1+C))-(Arf/2);
Electro_F = 2*sig_m* Vrms^4*M_Factor*0.125/(pi^2*Thc_m*R^2);
V_Th = Electro_F*(1e-6)^2/Vis;
figure (1)
```

```
hold on, grid on, box on
plot (log10(ome), V_Th, 'Line Width', 1.5)%, 'Marker', 'o'
xlabel ('Log Frequency')
ylabel ('The Time Average Fluid Velocity (ms-1)')
legend ('Fluid velocity induced by electrothermal body force')
```

IV-4. CM Factor Simulation

(Our collaborator Mr. Minglin Li developed this CM factor simulation program.)

```
clc, clear
% define the colours of output lines
str = ['b'; 'r'; 'c'; 'm'; 'g'];
% define the relative dielectric constant of the shell, the core,
% and the medium.
eps_sh = [6.1 70 70 70 50];
eps_cr = [6.9 1 1 1 1];
eps_m = [80 80 80 80 80];
% define the conductivity of the shell, the core and the medium
sig_sh = [1e-6 1e-6 1e-6 1e-6 1e-6]*1e-4;
sig_cr = [45.2e6 1e-2 1e-2 1e-2 1e7];
sig_m = [5e-5 5e-5 5.5e-6 5.5e-6 1e-2];
% define the radius of the particle and the core
radi.o = 12e-9;
radi.i = 10e-9;

for j = 2:2
   eps_r.sh = eps_sh(j);
   eps_r.cr = eps_cr(j);
   eps_r.m = eps_m(j);
   sig.sh = sig_sh(j);
   sig.cr = sig_cr(j);
   sig.m = sig_m(j);
   goldshell(str(j), eps_r, sig, radi);
   end

function [w,CM]=goldshell (str, eps_r, sig, radi)
% applied frequencies of the electric field
ome = [1:20:3e3,3e3:300:3e5,3e5:1e3:1e8,1e8:1e5:1e10];
```

```
%ome = [1:50:8000,8000:200:10000, 3e4, 1e5, 3e5, 1e6, 3e6, 1e7, 1e8];
eps_0 = 8.85e-12;
% Input the permittivity of the shell, the core and the medium
eps_sh = eps_r.sh*eps_0;
eps_cr = eps_r.cr*eps_0;
eps_m = eps_r.m*eps_0;
% Input the conductivity of the shell, the core and the medium
sig_sh = sig.sh;
sig_cr = sig.cr;
sig_m = sig.m;
% Input the radius of the whole particle and the core.
rad_o = radi.o;
rad_i = radi.i;
a = rad_o/rad_i;
% construct the complex permittivity of the shell, the core and the
% medium.
ceps_sh = eps_sh-i*sig_sh./ome;
ceps_cr = eps_cr-i*sig_cr./ome;
ceps_m = eps_m-i*sig_m./ome;
% calculate the complex CM factor
ceps_p = ceps_sh.*(a^3+2*(ceps_cr-ceps_sh)./(ceps_cr+2*ceps_sh))...
    ./(a^3-(ceps_cr-ceps_sh)./(ceps_cr+2*ceps_sh));
CM = (ceps_p-ceps_m)./(ceps_p+2*ceps_m);

figure (3)
%10 -2 100-1
hold on, grid on, box on
plot (log10(ome), real(CM), 'Colour', str, 'Line Width', 1.5)%, 'Marker', 'o'
xlabel ('Log Frequency')
ylabel ('Real component of CM factor')
```

IV-5. Particle velocity induced by DEP force

```
function [w, CM] = gDEP(str, eps_r, sig, radi)
% applied frequencies of the electric field
ome = [1:20:3e3,3e3:300:3e5,3e5:1e3:1e8,1e8:1e5:1e10];
%ome = [1e3:100:1e7];
```

```
%ome = [1:50:8000,8000:200:10000,3e4,1e5,3e5,1e6,3e6,1e7,1e8];
eps_0 = 8.85e-12;
% Input the permittivity of the shell, the core and the medium
eps_sh = eps_r.sh*eps_0;
eps_cr = eps_r.cr*eps_0;
eps_m = eps_r.m*eps_0;
% Input the conductivity of the shell, the core and the medium
sig_sh = sig.sh;
sig_cr = sig.cr;
sig_m = sig.m;
% Input the radius of the whole particle and the core.
rad_o = radi.o;
rad_i = radi.i;
a = rad_o/rad_i;
% construct the complex permittivity of the shell, the core and the
% medium.
ceps_sh = eps_sh-i*sig_sh./ome;
ceps_cr = eps_cr-i*sig_cr./ome;
ceps_m = eps_m-i*sig_m./ome;
% calculate the complex CM factor
ceps_p = ceps_sh.*(a^3+2*(ceps_cr-ceps_sh)./(ceps_cr+2*ceps_sh))...
      ./(a^3-(ceps_cr-ceps_sh)./(ceps_cr+2*ceps_sh));
CM = (ceps_p-ceps_m)./(ceps_p+2*ceps_m);
% Gobal variables
Pi = 3.14;
Vis = 8.9e-4; % Viscosity of the medium
Vrms = 14; % RMS of input voltage
% Calculate particle velocity generated by DEP force
Erms = 32*((Vrms/sqrt(2))/(2e-6)^2)^2*0.7e-6;
DEP_Force = real(CM)*2*Pi*rad_o*rad_o*rad_o*Erms*eps_m;
DEP_V = DEP_Force/(6*3.14*Vis*rad_o);
figure (1)
hold on, grid on, box on
plot (log10(ome), DEP_V, 'Colour', str, 'Line Width', 1.5)%, 'Marker', 'o'
xlabel ('frequency (log) Hz')
ylabel ('The Particle Velocity (ms-1)')
legend ('Particle velocity induced by DEP force')
```